Editors' Suggestion

Universality of point defect structure in body-centered cubic metals

Pui-Wai Ma* and S. L. Dudarev

CCFE, Culham Science Centre, UK Atomic Energy Authority, Abingdon, Oxfordshire OX14 3DB, United Kingdom

(Received 20 September 2018; published 10 January 2019)

Formation and migration energies, elastic dipole, and relaxation volume tensors of nanodefects are the parameters determining the rates of evolution of microstructure under irradiation as well as macroscopic elastic stresses and strains resulting from the accumulation of defects in materials. To find the accurate values of these parameters, we have performed density functional theory simulations of self-interstitial and vacancy defects in all the body-centred cubic metals, including alkaline metals (Li, Na, K, Rb and Cs), alkaline-earth metal (Ba), nonmagnetic transition metals (V, Nb, Mo, Ta and W), and magnetic transition metals (Cr and Fe), correcting the computed values for the effect of finite cell size and periodic boundary conditions. The lowest energy structure of a self-interstitial atom defect is universal to all the nonmagnetic bcc metals, including metals of groups 1 and 2 of the periodic table, and has the $\langle 111 \rangle$ symmetry. The only exceptions are the $\langle 110 \rangle$ self-interstitial defect configuration in Fe, and a $\langle 11\xi \rangle$ configuration in Cr. We have also computed elastic dipole tensors and relaxation volumes of self-interstitial and vacancy defects in all the bcc metals and explored how elastic relaxation parameters vary along the defect migration pathways.

DOI: 10.1103/PhysRevMaterials.3.013605

I. INTRODUCTION

Dislocations and point defects in crystalline materials are created by mechanical deformation or by irradiation, followed by the relaxation of locally distorted atomic configurations [1]. A Frenkel pair is a commonly occurring type of radiation defect. In a Frenkel pair, an atom is removed from a lattice site and placed elsewhere in the lattice, forming a pair of a vacancy and a self-interstitial atom (SIA) defect. In elasticity theory, the strain field associated with a defect can be described by its elastic dipole tensor [2–7]. Matrix elements of elastic dipole tensor can be derived from atomic scale simulations, where interatomic forces are evaluated using empirical potentials or *ab initio* methods. Using elastic dipole tensors, discrete atomic configurations of defects can be treated as objects of continuum elasticity, enabling simulations of evolution of large ensembles of defects on the time and spatial scales many orders of magnitude larger than those accessible to molecular dynamics or electronic structure based methods [8].

The dipole tensor of a defect P_{ij} fully defines its properties within the theory of elasticity [9]. The energy of elastic interaction between a defect and an external strain field $\epsilon_{ij}^{\text{ext}}$ is

$$E_{\text{int}}^{\text{ext}} = -P_{ij}\epsilon_{ij}^{\text{ext}}, \tag{1}$$

whereas the energy of interaction between two defects separated by a distance many times their size is

$$E_{\text{int}}^{ab} = P_{ij}^{a} P_{kl}^{b} \frac{\partial^2}{\partial x_j \partial x_l} G_{ik}(\mathbf{r}), \tag{2}$$

where P_{ij}^{a} and P_{kl}^{b} are the dipole tensors of defects a and b, $\mathbf{r}$ is the relative position vector of the defects, and G_{ik} is the elastic Green's function. G_{ik} can be evaluated numerically for an arbitrary elastically anisotropic material [10] from the matrix elements of the stiffness tensor. Using Eq. (2), the energy of elastic interaction can be computed for any configuration of defects, which otherwise is difficult to treat using atomistic or electronic structure based methods due to the limitations imposed by the simulation cell size.

Domain and Becquart [11] computed the dipole tensor of a vacancy (using an *ab initio* approach) and an SIA (using empirical potentials) in iron using the Kanzaki force formalism. Varvenne and Clouet [6] showed how to evaluate the dipole tensor of a defect from average macrostresses in a simulation cell and investigated the numerical convergence of calculations as a function of cell size. Treating point defects in zirconium, they compared the rate of convergence of the two methods and showed that the Kanzaki force and macrostress approaches produced similar results in the limit where simulation cells were sufficiently large.

Sivak *et al.* [12] investigated elastic interactions between point defects and dislocations in iron, computing them using molecular statics and linear elasticity. Matrix elements of dipole tensors of defects were derived from atomistic calculations, where interaction between the atoms was described by empirical interatomic potentials. They found that the elasticity approximation described the energy of interaction fairly well if a defect and a dislocation line were separated by a distance just a little over three lattice constants, in agreement with the analysis of dislocation core effects by Boleininger *et al.* [13]. Sivak *et al.* [12] also evaluated elastic dipole tensors of vacancies and SIA defects in iron at equilibrium and at saddle points.

Since the elastic energy of interaction between a defect and external strain field can be readily evaluated using the dipole

*Corresponding author: Leo.Ma@ukaea.uk

tensor formalism, elastic interaction effects can be included in coarse-grained models, for example in object kinetic Monte Carlo (kMC). By performing kMC simulations, Sivak *et al.* estimated the effect of elastic interactions on the diffusion of defects in bcc iron and vanadium [14], and also on the diffusion of hydrogen in bcc iron [15,16]. They concluded, in agreement with the earlier works by Margvelashvili and Saralidze [17], Wolfer and Ashkin [18], and Brailsford and Bullough [19] that dislocations were more efficient sinks for SIA defects than for vacancies. The sink strength of an edge dislocation was several times larger than that of a screw dislocation for both SIA and vacancy defects in Fe and V. Assessing the effect of elastic field of a dislocation on the diffusion of a hydrogen interstitial, they showed that the predicted sink strength efficiency was relatively high for an edge dislocation, but was significantly lower for a screw dislocation.

This brings into focus the question about the structure of a defect in a metal. Paneth [20] suggested that in an alkaline metal, an SIA defect would adopt a ⟨111⟩ configuration. He evaluated the formation energy of a ⟨111⟩ crowdion in sodium using a model where a positive point charge was embedded in a uniform field of negative charge density, and found the formation energy of the defect to be close to 0.3 eV. Below, we show that a more reliable value can now be derived from density functional theory (DFT) calculations.

Other researchers later argued that it was the ⟨110⟩ dumbbell that represented the most stable SIA defect configuration in Fe and Mo [3,21]. This assertion was based on the data derived from the analysis of diffuse x-ray scattering experiments. Interpreting diffuse x-ray diffraction data in definitive terms is difficult since even at cryogenic temperatures radiation induced defects diffuse [22], interact and can form fairly complex clusters.

Depending on the structure of an SIA configuration, SIA defects have different mobilities. A ⟨111⟩ defect can easily translate itself through the lattice in the direction parallel to its axis, suggesting that a ⟨111⟩ crowdion should be highly mobile even at fairly low temperatures [22,23]. This explains the high diffusivity of SIAs observed in resistivity recovery experiments performed on electron irradiated bcc metals [24–26]. Experimental observations, confirmed by theoretical analysis [22], show that in many bcc metals SIA defects still move at temperatures below 6 K. High-voltage electron microscope experiments [27] also show that the activation energy characterizing long-range migration of SIA defects in tungsten is low. On the other hand, a ⟨110⟩ dumbbell in Fe migrates through a sequence of translation and rotational jumps [3,28], and its three-dimensional diffusion is strongly thermally activated. *Ab initio* DFT calculations have been recently applied to the evaluation of formation and migration energies of defects in bcc metals and to the calculation of relaxation volumes of defects [29–38]. In all the nonmagnetic (NM) bcc transition metals, the most stable SIA defect structure was found to have the ⟨111⟩ symmetry [30,31]. Swinburne *et al.* [22] showed that the migration energy of a ⟨111⟩ dumbbell in tungsten is close to 2 meV, and that the saddle point configuration on a defect migration pathway is a ⟨111⟩ crowdion. Quantum fluctuations of atomic positions make the ⟨111⟩ SIA defects extremely mobile at temperatures as low as 1 K [22].

The only *ab initio* study of SIA defects in alkaline metals carried out so far was performed by Breier *et al.* [32]. They evaluated the formation energies of ⟨111⟩, ⟨110⟩, and ⟨100⟩ SIA dumbbells in sodium, computing them using DFT in the local density approximation (LDA). The ⟨110⟩ dumbbell was found to have the lowest energy, although it was only 0.01eV lower than that of the ⟨111⟩ dumbbell configuration. Calculations in Ref. [32] were performed using a relatively small 55-atom cell. Below, we compare these results with calculations performed using more accurate density functionals and larger simulation cells. We also investigate the structure of defects in all the other bcc metals in the periodic table, including alkaline metals. In iron, the ⟨110⟩ dumbbell is the most stable SIA configuration [11,30,31]. The three-dimensional translation-rotation migration pathway of the defect [29] explains the relatively high activation temperature for the onset of diffusion of SIAs in iron [24,25,28], which is close to 120 K.

The structure of an SIA defect in chromium remains somewhat uncertain. Calculations assuming a NM electronic ground state [30,31] or an antiferromagnetic (AFM) state [39,40] showed that the difference between the formation energies of ⟨111⟩ and ⟨110⟩ dumbbells was within the margin of error of *ab initio* calculations. Recently, we found [41] that the most stable configuration of an SIA defect in Cr has the ⟨11ξ⟩ orientation, where ξ varies from 0.355 to 0.405, regardless of magnetic order.

In this paper, in addition to determining the structure and energies of various defect configurations, we have also evaluated their elastic properties needed for large-scale dynamic simulations of microstructure [42]. We start by computing the formation and migration energies of defects, treating interactions with periodic images in the linear elasticity approximation. Then, we evaluate dipole tensors and relaxation volume tensors of all the defect structures in all the bcc metals, including alkaline metals Li, Na, K, Rb, and Cs, alkaline-earth metal Ba, NM transition metals V, Nb, Mo, Ta, and W, and magnetic transition metals Cr and Fe. Thermal migration of a ⟨111⟩ SIA defect proceeds through a sequence of ⟨111⟩ crowdion ↔ ⟨111⟩ dumbbell transformations. This involves almost no variation of the elastic dipole tensor. On the other hand, when investigating the migration of a ⟨110⟩ defect configuration in Fe, we find that it involves some significant variation of the dipole tensor along the migration pathway.

II. THEORY

We start by briefly reviewing the methodology for computing the formation and migration energies of defects, dipole, and relaxation volume tensors, and the variation of these quantities along defect migration pathways.

The formation energy of a defect $E^F_{\rm def}$ is

$$E^F_{\rm def} = E_{\rm def}(N_{\rm def}) - \frac{N_{\rm def}}{N_{\rm bulk}} E_{\rm bulk}(N_{\rm bulk}), \tag{3}$$

where $E_{\rm def}$ is the energy of a simulation cell containing a defect, $E_{\rm bulk}$ is the energy of a reference defect-free cell, and $N_{\rm def}$ and $N_{\rm bulk}$ are the numbers of atoms in the respective cells.

Equation (3) leaves open the question about whether the simulation cell should be fully relaxed or the relaxation of ion positions should be performed in a constrained manner,

leaving the boundaries of the cell fixed. The subtlety of Eq. (3) is also associated with the fact that it implicitly assumes the limit $N_{\rm def}, N_{\rm bulk} \to \infty$. Equation (3) defines the formation energy of a defect, assuming that the defect is embedded in an infinite medium, an approximation that is not satisfied in a practical simulation. To circumvent the need to treat the surface termination effect, simulations of defects are performed using periodic boundary conditions. This is equivalent to evaluating the energy associated with embedding an infinite number of defects in an infinite medium. Naturally, to relate the formation energy defined by Eq. (3) to a calculation performed using periodic boundary conditions, it is necessary to subtract from the result of an *ab initio* calculation the energy of interaction between a defect and all its periodic images, and estimate the contribution associated with the lattice deformation generated by the infinite number of images of the defect.

An alternative approach is to relax the orientation and position of boundaries of the cell to arrive at a stress-free state of the material. Varvenne *et al.* [5,6] noted that the stress-free approach exhibited better numerical convergence as a function of the simulation cell size, and produced lower values of formation energies. Relaxing positions and orientations of boundaries of the simulation cell containing a defect is equivalent to applying a homogeneous elastic strain $\boldsymbol{\epsilon}^{\rm app}$. The elastic energy associated with this strain $E^{\rm app}$ contributes to the formation energy of the defect.

The strain tensor $\boldsymbol{\epsilon}^{\rm app}$ associated with the relaxation of boundaries of the simulation cell satisfies the condition

$$\mathbf{V}^{\rm ref}(\mathbf{I} + \boldsymbol{\epsilon}^{\rm app}) = \mathbf{V}^{\rm def}, \tag{4}$$

where $\mathbf{I}$ is the identity matrix, $\mathbf{V}^{\rm ref} = \{\mathbf{L}_1^{\rm ref}, \mathbf{L}_2^{\rm ref}, \mathbf{L}_3^{\rm ref}\}$ is the matrix of translation vectors of the reference cell and $\mathbf{V}^{\rm def} = \{\mathbf{L}_1^{\rm def}, \mathbf{L}_2^{\rm def}, \mathbf{L}_3^{\rm def}\}$ is the matrix of translation vectors of the cell containing a defect. The elastic energy associated with the applied strain $\boldsymbol{\epsilon}^{\rm app}$ is [5]

$$E^{\rm app} = \frac{V^{\rm ref}}{2} C_{ijkl} \epsilon_{ij}^{\rm app} \epsilon_{kl}^{\rm app} - P_{ij} \epsilon_{ij}^{\rm app}, \tag{5}$$

where $V^{\rm ref}$ is the volume of the simulation cell and C_{ijkl} is the elastic constant tensor. The quadratic term in Eq. (5) is the elastic energy associated with the deformation of the simulation box, whereas the second term is the energy of interaction between the defect and the applied strain. Since Eq. (5) is valid in the limit $\|\epsilon^{\rm app}\| \ll 1$, we neglect the difference between the volume of the reference cell and the cell containing a defect.

Equation (3) for the formation energy of a defect now has the form

$$E_{\rm def}^{F} = [E_{\rm def}(N_{\rm def}) - E^{\rm app}] - \frac{N_{\rm def}}{N_{\rm bulk}} E_{\rm bulk}(N_{\rm bulk}) - E_{\rm el}^{\rm corr}, \tag{6}$$

where $E_{\rm el}^{\rm corr}$ is a term taking into account the elastic field of the defect and its interaction with its periodically translated images. This elastic correction is a sum of two parts,

$$E_{\rm el}^{\rm corr} = E_{\rm int} + E_{\rm strain}^{\rm corr}, \tag{7}$$

where $E_{\rm int}$ is the elastic energy of interaction with periodic images of the defect. $E_{\rm int}$ can be computed in the elastic dipole approximation. $E_{\rm strain}^{\rm corr}$ is the self-strain correction energy associated with the regularization of strain $\epsilon_{ij}^{D}(\mathbf{r})$ produced by the defect in the simulation cell itself. This regularization is required to make $\epsilon_{ij}^{D}(\mathbf{r})$ compatible with the fact that under the condition of no overall relaxation of the simulation cell, the total macroscopic strain must vanish [7].

The above consideration also applies to any configuration related to the lowest energy defect structure through an adiabatic transformation. Equation (6) remains valid at any point on a migration pathway of a defect found using an NEB calculation.

Numerical values of $E_{\rm int}$ can be computed from the dipole tensor of the defect and the anisotropic elastic Green's function of the crystal [4–7]. The regularized energy of elastic interaction between a defect and its periodic images, compatible with the condition of zero average elastic strain, is [7]

$$E_{\rm int} = E_{\rm int}^{\rm total} + E_{\rm int}^{\rm corr}, \tag{8}$$

where

$$E_{\rm int}^{\rm total} = \frac{1}{2} \sum_{n \neq 0} P_{ij} P_{kl} \frac{\partial}{\partial x_j} \frac{\partial}{\partial x_l} G_{ik}(\mathbf{R}_n) \tag{9}$$

$$= \frac{1}{2} \sum_{n \neq 0} P_{ij} P_{kl} G_{ik,jl}(\mathbf{R}_n) \tag{10}$$

is a conditionally convergent sum of pairwise elastic interactions between a defect and its periodic images situated at $\mathbf{R}_n$. The term

$$E_{\rm int}^{\rm corr} = -\frac{1}{2V_{\rm cell}} \sum_{n \neq 0} \int_{V_{\rm cell}} P_{ij} P_{kl} G_{ik,jl}(\mathbf{R}_n - \mathbf{r}) d^3 r \tag{11}$$

regularizes the strain produced by the periodic images and ensures the absolute convergence of the sum Eq. (10). The self-strain correction energy is

$$E_{\rm strain}^{\rm corr} = -\frac{1}{2} P_{ij} \left(-\bar{\epsilon}_{ij}^{D}\right) = \frac{P_{ij}}{2V_{\rm cell}} \int_{V_{\rm cell}} \epsilon_{ij}^{D}(\mathbf{r}) d^3 r. \tag{12}$$

Since in a DFT calculation we do not explicitly compute $\epsilon_{ij}^{D}(\mathbf{r})$, and only need to correct the *elastic* part of the strain field of the defect, we again use the dipole tensor approximation and write

$$E_{\rm strain}^{\rm corr} = -\frac{1}{2V_{\rm cell}} \int_{V_{\rm cell}} P_{ij} P_{kl} G_{ik,jl}(\mathbf{r}) d^3 r. \tag{13}$$

This term corrects the total energy for the effect of elastic strain produced by the defect itself. The correction has the same form as Eq. (11), and corresponds to the first term of the series $n = 0$.

Numerically, Eqs. (11) and (13) can be conveniently represented by surface integrals through the use of the divergence theorem [43], namely

$$\int_{V_{\rm cell}} P_{kl} G_{ik,jl}(\mathbf{r}) d^3 r = \oint_{S_{\rm cell}} P_{k\alpha} G_{ik,j}(\mathbf{r}) n_\alpha dS. \tag{14}$$

Here $\mathbf{n}$ is the unit vector of external surface normal, and α denotes a Cartesian component of this vector. Evaluating the first derivative of Green's function $G_{ik,j}(\mathbf{r})$ is numerically more expedient than the second derivative $G_{ik,jl}(\mathbf{r})$. Numerical tests show that the results obtained using the above equations are in

TABLE I. Elastic constants (in GPa units) calculated using the Le Page and Saxe [59] method for a two-atom cell, using a 30 × 30 × 30 k-points mesh, and GGA-PBE exchange-correlation functional. Atomic volumes (Å^3) and lattice constants (Å) were taken from relaxed 128 atoms perfect lattice simulations. Numbers in italic are experimental values. Numbers in bold were computed using the AM05 exchange-correlation functional.

	C_{11} (GPa)	C_{12} (GPa)	C_{44} (GPa)	Ω_0 (Å^3)	a_0 (Å)
Li	18.14	11.85	11.43	20.24	3.434
	14.85[a]	*12.53*[a]	*10.80*[a]	*21.27*[b]	*3.491*[b]
Na	9.34	7.44	5.96	36.94	4.196
	8.57[c]	*7.11*[c]	*5.87*[c]	*37.71*[b]	*4.225*[b]
K	3.91	3.44	2.70	73.63	5.281
	4.17[d]	*3.41*[d]	*2.86*[d]	*71.32*[b]	*5.225*[b]
Rb	3.07	2.65	1.99	90.92	5.665
	3.25[e]	*2.73*[e]	*1.98*[e]	*87.10*[b]	*5.585*[b]
Cs	2.16	1.85	1.38	116.74	6.158
	2.47[f]	*2.06*[f]	*1.48*[f]	*110.45*[b]	*6.045*[b]
Ba	12.06	7.31	10.39	63.55	5.028
	13.0[g]	*7.6*[g]	*11.8*[g]	*63.25*[b]	*5.02*[b]
V	279.59	142.02	26.72	13.40	2.993
	308.53	**147.96**	**31.31**	**12.91**	**2.955**
	227.9[h]	*118.7*[h]	*42.6*[h]	*13.91*[b]	*3.03*[b]
Nb	248.76	135.24	19.46	18.33	3.322
	273.54	**143.06**	**23.62**	**17.68**	**3.282**
	246.6[h]	*133.2*[h]	*28.1*[h]	*17.97*[b]	*3.30*[b]
Mo	469.07	157.72	99.71	15.77	3.160
	505.43	**175.26**	**108.04**	**15.24**	**3.124**
	464.7[h]	*161.5*[h]	*108.9*[h]	*15.63*[h]	*3.15*[b]
Ta	266.28	161.36	76.75	18.29	3.320
	293.44	**168.18**	**82.08**	**17.62**	**3.278**
	266.0[h]	*161.2*[h]	*82.4*[h]	*17.97*[b]	*3.30*[b]
W	518.26	199.77	142.09	16.14	3.184
	569.73	**211.52**	**157.16**	**15.61**	**3.149**
	522.4[h]	*204.4*[h]	*160.6*[h]	*15.78*[b]	*3.16*[b]
Cr	448.12	62.03	102.13	11.72	2.862
	394.1[i]	*88.5*[i]	*103.75*[i]	*11.94*[b]	*2.88*[b]
Fe	289.34	152.34	107.43	11.34	2.831
	243.1[j]	*138.1*[j]	*121.9*[j]	*11.82*[b]	*2.87*[b]

[a]Ref. [64].
[b]Ref. [65].
[c]Ref. [66].
[d]Ref. [67].
[e]Ref. [68].
[f]Ref. [69].
[g]Ref. [70].
[h]Ref. [71].
[i]Ref. [72].
[j]Ref. [73].

agreement with calculations performed using code ANETO developed by Varvenne *et al.* [5].

The dipole tensor of a localized defect can be calculated from macrostresses developing in a simulation box due to the presence of a defect [5,7]. The calculation is exact if all the nonlinear deformations associated with the defect structure are contained entirely within the cell [7], even if the cell size is relatively small. The dipole tensor is computed

TABLE II. The total energy $E_{\rm def}$ of a simulation cell containing a defect, the applied strain energy $E^{\rm app}$, the elastic correction energy $E^{\rm corr}_{\rm el}$, and the formation energy $E^{F}_{\rm def}$ of a defect in W, where the total energy of a perfect lattice cell is $E_{\rm bulk} = -1658.68112$eV. The values are computed using 4×4×4 unit cells. The shape and the volume of simulation cells containing defects are the same as those of the perfect lattice cell, with no relaxation of boundary conditions. All the values are given in eV units.

W	$E_{\rm def}$	$E^{\rm app}$	$E^{\rm corr}_{\rm el}$	$E^{F}_{\rm def}$
⟨111⟩d	−1661.142709	0.0000	0.2101	10.2867
⟨111⟩c	−1661.140788	0.0000	0.2100	10.2888
⟨110⟩d	−1660.823317	0.0000	0.2401	10.5761
Tetra	−1659.652937	0.0000	0.2697	11.7169
⟨100⟩d	−1659.149546	0.0000	0.2941	12.1959
Octa	−1659.074298	0.0000	0.3001	12.2652
Vac	−1642.491107	0.0000	0.0083	3.2233

using the equation [4–7]

$$P_{ij} = V_{\rm cell}\left(C_{ijkl}\epsilon^{\rm app}_{kl} - \bar{\sigma}_{ij}\right), \tag{15}$$

where

$$\bar{\sigma}_{ij} = \frac{1}{V_{\rm cell}}\int_{V_{\rm cell}} \sigma_{ij} dV \tag{16}$$

is the average macroscopic stress in the simulation box. The relaxation volume tensor of a defect, proportional to the so-called λ-tensor [2], is defined as

$$\Omega_{ij} = S_{ijkl} P_{kl}, \tag{17}$$

where $\mathbf{S} = \mathbf{C}^{-1}$ is the elastic compliance tensor, satisfying the condition $C_{ijkl}S_{klmn} = \frac{1}{2}(\delta_{im}\delta_{jn} + \delta_{in}\delta_{jm})$. The relaxation volume of the defect can be computed by taking the trace of tensor Ω_{ij}, namely

$$\Omega_{\rm rel} = Tr\Omega_{ij} = \Omega_{11} + \Omega_{22} + \Omega_{33}. \tag{18}$$

In the next section, we summarize the results of *ab initio* calculations of energies and elastic properties of defects in

TABLE III. The total energy $E_{\rm def}$ of a simulation cell containing a defect, the applied strain energy $E^{\rm app}$, the elastic correction energy $E^{\rm corr}_{\rm el}$, and the formation energy $E^{F}_{\rm def}$ of a defect in W, where the total energy of a perfect lattice cell is $E_{\rm bulk} = -1658.68112$eV. The values are computed using 4×4×4 unit cells. The shape and the volume of simulation cells containing defects are relaxed to the stress-free condition. All the values are given in eV units.

W	$E_{\rm def}$	$E^{\rm app}$	$E^{\rm corr}_{\rm el}$	$E^{F}_{\rm def}$
⟨111⟩d	−1661.631853	−0.4825	0.2063	10.2839
⟨111⟩c	−1661.630294	−0.4832	0.2060	10.2864
⟨110⟩d	−1661.226956	−0.3991	0.2319	10.5798
Tetra	−1660.049231	−0.3938	0.2652	11.7190
⟨100⟩d	−1659.579432	−0.4271	0.2861	12.2012
Octa	−1659.509293	−0.4320	0.2930	12.2693
Vac	−1642.502871	−0.0130	0.0085	3.2242

TABLE IV. Formation energies E^F (in eV units) of various self-interstitial atom (SIA) configurations and a vacancy in bcc metals, computed using the GGA-PBE functional. An SIA defect may adopt a ⟨111⟩ dumbbell, ⟨111⟩ crowdion, ⟨110⟩ dumbbell, tetrahedral site interstitial, ⟨100⟩ dumbbell, and octahedral site interstitial configuration. In antiferromagnetic chromium, a ⟨11ξ⟩ ($\xi \approx 0.355$) dumbbell is the most stable SIA configuration.

PBE	Li	Na	K	Rb	Cs	Ba	V	Nb	Mo	Ta	W	Cr	Fe
⟨111⟩d	0.573	0.510	0.458	0.423	0.426	1.518	2.407	3.949	7.475	4.773	10.287	6.617	5.090
⟨111⟩c	0.575	0.510	0.451	0.430	0.427	1.518	2.412	3.948	7.479	4.774	10.289	6.555	5.093
⟨110⟩d	0.637	0.540	0.483	0.464	0.446	1.765	2.676	4.204	7.580	5.479	10.576	6.515	4.321
Tetra	0.696	0.582	0.520	0.492	0.480	1.724	2.898	4.422	8.358	5.770	11.717	6.918	4.790
⟨100⟩d	0.782	0.667	0.606	0.564	0.556	1.831	2.833	4.502	8.890	5.889	12.196	7.275	5.463
Octa	0.785	0.663	0.612	0.566	0.560	1.858	2.895	4.618	8.916	5.946	12.265	7.354	5.555
Vac	0.488	0.341	0.305	0.269	0.255	1.019	2.036	2.646	2.787	2.864	3.223	3.004	2.190
⟨11ξ⟩d												6.361	

all the bcc metals in the Periodic table, including alkaline, alkaline-earth, and transition $3d$, $4d$, and $5d$ metals.

III. EQUILIBRIUM CONFIGURATIONS OF DEFECTS

The *ab initio* calculations described below were performed using Vienna *ab initio* Simulation Package (VASP) [44–47]. We use supercells containing $4 \times 4 \times 4$ bcc unit cells and a $5 \times 5 \times 5$ k-point mesh. The plane wave energy cutoff for Li was chosen at 1500 eV, for Na and K at 780 eV, for Rb and Cs at 660 eV, for Ba at 560 eV, and for all the other elements at 450 eV. We used the projector augmented-wave method potentials [48,49] and the GGA-PBE [50] exchange-correlation functional. Defects in NM transition metals were also explored using the AM05 exchange-correlation functional [51–53]. There are 3, 7, 9, 9, 9, and 10 valence electrons per atom in Li, Na, K, Rb, Cs, and Ba, and 11, 12, 14, 11, 12, 11, and 12 valence electrons per atom in V, Cr, Fe, Nb, Mo, Ta, and W, respectively.

Calculations of defect structures in Cr and Fe were performed in the collinear magnetic approximation. Otherwise, we assumed the metals to be NM, in agreement with experimental observations. The ground state of Cr was assumed to be AFM. A detailed analysis shows that the true electronic ground state of Cr has the form of a spin density wave (SDW) [54], but within the error margin of *ab initio* calculations the energy of this SDW state is practically indistinguishable from that of the AFM state [55]. All the calculations for Fe were performed assuming a collinear ferromagnetic (FM) electronic ground state [56,57]. We note that in principle, noncollinear magnetic configurations may form, due to the spin-orbit coupling effect, in the vicinity of defects where the atomic lattice is strongly distorted. The magnitude of spin-orbit coupling increases rapidly as a function of atomic number [58], and does not play a significant part in the relatively light elements like Fe. On the other hand, heavier metals like tungsten are NM, which justifies neglecting the spin-orbit coupling effect in density functional calculations performed here.

Calculations were performed as follows. For each metal, we relaxed a simulation cell containing 128 atoms arranged in a perfect bcc lattice structure, and computed the equilibrium lattice constant. Then, by inserting an extra atom in the simulation cell, we formed various SIA configurations, including a ⟨111⟩ dumbbell, a ⟨111⟩ crowdion, a ⟨110⟩ dumbbell, a tetrahedral site interstitial, a ⟨100⟩ dumbbell, and an octahedral site interstitial, or created a vacancy by removing an atom from a lattice site. Ion positions were then relaxed without altering the shape and volume of the simulation cell. The convergence condition was defined by the maximum force acting on any atom in the cell, which was set to be less than 0.01 eV/Å.

To evaluate the relaxation volume tensor of a defect, we require the compliance tensor S_{klmn}, which can be computed from the elastic constant tensor C_{ijkl}. Elastic constant tensors C_{ijkl} for various metals were computed using the Le Page and Saxe method [59], using a two-atom simulation cell and a $30 \times 30 \times 30$ k-point mesh. The atomic volume Ω_0 and the equilibrium lattice constant a_0 for each metal were derived from a 128 atom cell perfect lattice calculation. The results are summarized in Table I together with experimental data. The calculated values are generally in agreement with experimental data.

To verify the validity of Eq. (6), we use tungsten as an example. We compute $E_{\rm def}$, $E^{\rm app}$, $E_{\rm el}^{\rm corr}$, and $E_{\rm def}^F$ for a vacancy and various SIA configurations, using relaxed and unrelaxed simulation cells. Tables II and III show that the computed formation energies of point defects $E_{\rm def}^F$ are compatible with each other. The values of $E_{\rm def}$ can vary significantly if the simulation cell is relaxed arbitrarily without considering elastic corrections. On the other hand, the values of defect formation energies $E_{\rm def}^F$ in tungsten, computed using the relaxed and unrelaxed cell approaches, differ by less than 0.1%.

TABLE V. Formation energies E^F (in eV units) of various self-interstitial atom configurations and a vacancy in bcc nonmagnetic transition metals, computed using the AM05 functional.

AM05	V	Nb	Mo	Ta	W
⟨111⟩d	2.905	4.256	7.866	5.086	10.810
⟨111⟩c	2.913	4.255	7.869	5.088	10.812
⟨110⟩d	3.158	4.517	7.993	5.749	11.118
Tetra	3.421	4.768	8.808	6.085	12.302
⟨100⟩d	3.378	4.910	9.405	6.262	12.858
Octa	3.444	5.029	9.434	6.330	12.931
Vac	2.610	2.944	3.105	3.172	3.619

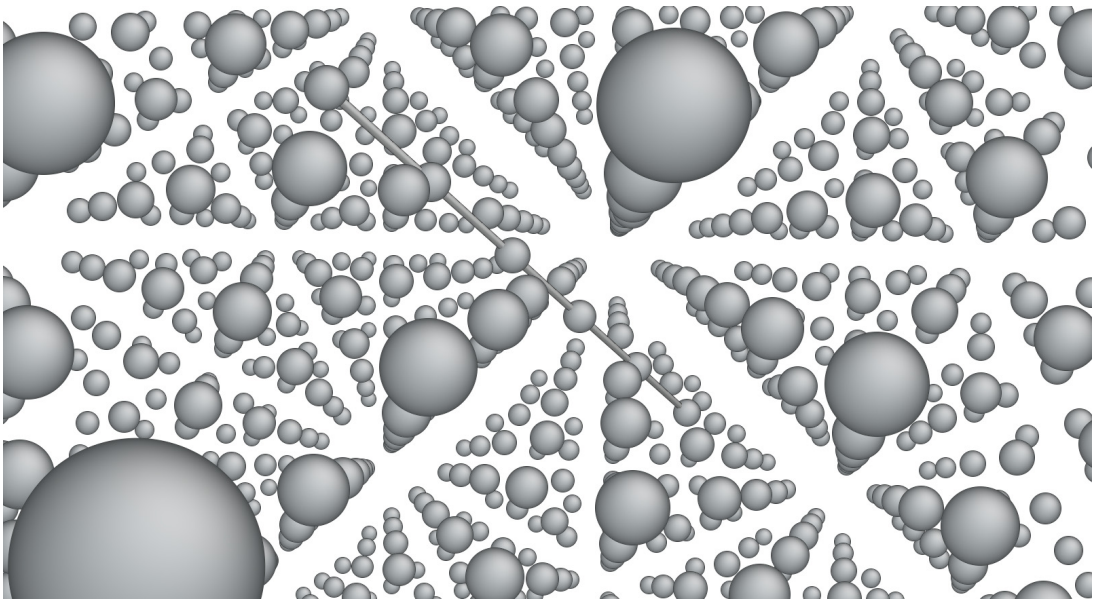

FIG. 1. Sketch of the atomic structure of a ⟨111⟩ self-interstitial atom dumbbell defect in a bcc metal.

In Tables IV and V, we summarize the computed formation energies of all the point defects in all the bcc metals. With the exception of magnetic transition metals Cr and Fe, self-interstitial defects in all the bcc metals universally adopt the ⟨111⟩ dumbbell or crowdion lowest energy configuration. A sketch of this universal ⟨111⟩-type self-interstitial defect structure is shown in Fig. 1.

The formation energies of defects given in Tables IV and V show that the difference between energies of the ⟨111⟩ dumbbell and crowdion configurations is in the meV range. A similar pattern of stability of defects was found by Nguyen-Manh *et al.* [30] and Derlet *et al.* [31] in NM transition metals. Our results for these metals agree with earlier calculations, and this is also confirmed by additional calculations performed using the AM05 functional. Furthermore, we find that the trend exhibited by configurations of defects in bcc alkaline and alkaline-earth metals remains the same as in NM bcc transition metals. The fact that the lowest energy configuration of a defect depends only on the crystal structure and does not depend, for example, on the directionality of bonding between the atoms in a metal is unexpected, and is one of the key findings of this paper.

Figure 2 shows a two-dimensional plot of electron charge density difference in sodium and tungsten, computed for a ⟨111⟩ dumbbell SIA defect in the $(\bar{2}11)$ plane. Electron charge density difference equals the fully convergent electron density computed *ab initio* minus the superposition of atomic charge densities. The two-dimensional plots show that interatomic bonding in the two metals differs significantly, and is mediated by *s* and *d* electrons, respectively. Still, the lowest-energy structure of the defect is the same in both metals. A defect forms an area of strong local deformation extended in the ⟨111⟩ direction. The distance between the atoms in a ⟨111⟩ strings is the shortest in bcc lattice. It appears that in W the defect structure is stabilized by the increase of electron density between atoms in the ⟨111⟩ string containing an extra atom,

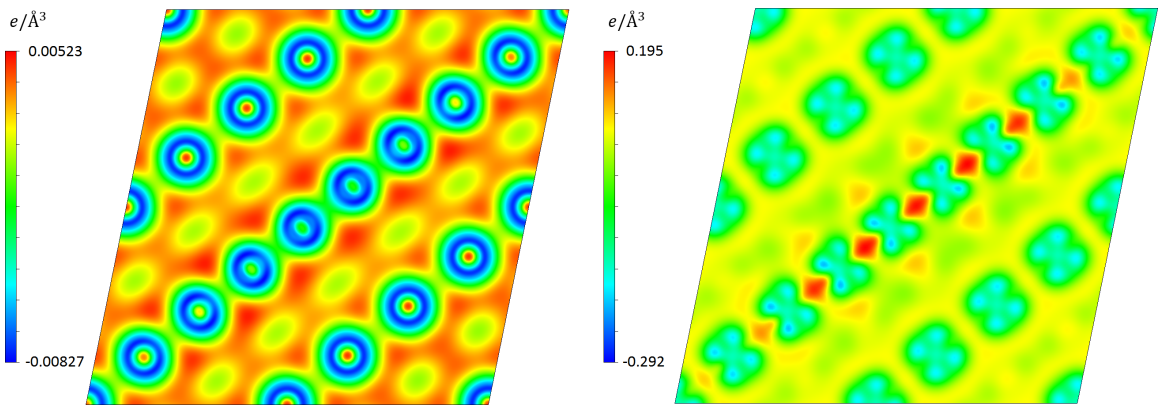

FIG. 2. Two-dimensional plots of electron charge density difference in sodium (left) and tungsten (right), computed for a ⟨111⟩ dumbbell SIA defect in the $(\bar{2}11)$ plane. Electron charge density difference equals the fully convergent electron density computed *ab initio* minus the superposition of atomic charge densities.

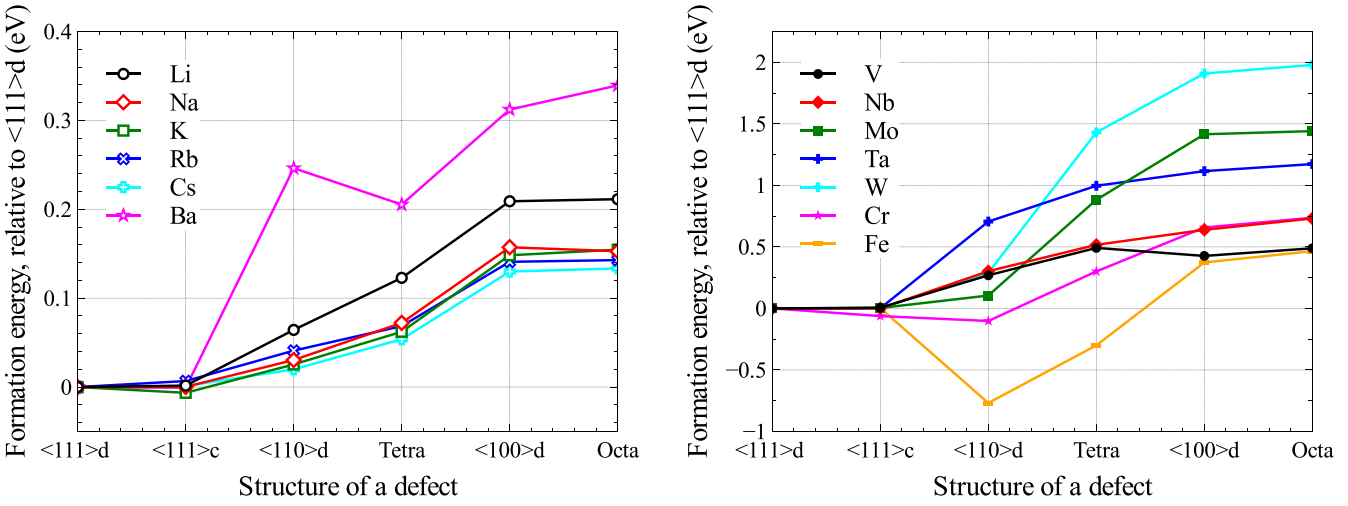

FIG. 3. Formation energies of various self-interstitial atom (SIA) defect configurations in bcc metals. Formation energies are given taking the formation energy of a ⟨111⟩ dumbbell as a reference for a given metal.

similar to bonds forming in a molecule [60]. In sodium, the charge density difference shows no evidence of directional or covalent molecular bonding, and the electronic phenomenon responsible for the anomalously high stability of the ⟨111⟩ defect structure appears elusive.

Figure 3 illustrates, in a graphical form, the data listed in Table IV. In the figure, all the values are shown relative to the ⟨111⟩ dumbbell formation energy. Figure 3 shows that in all the NM bcc metals, an SIA defect adopts either a ⟨111⟩ dumbbell or a ⟨111⟩ crowdion configuration as the lowest energy state. Swinburne *et al.* [22], using DFT and the nudge elastic band (NEB) method, showed that a ⟨111⟩ SIA in tungsten migrates through a sequence of dumbbell↔crowdion↔ dumbbell steps with a barrier that is as low as 2 meV. Given such a low migration barrier, it is hardly surprising that quantum fluctuations of atomic positions are able to assist the movement of an SIA through the lattice at very low temperatures [27]. The data given in Table IV explain why in many bcc metals, SIA defects are able to migrate at temperatures lower than 6 K, in agreement with resistivity recovery experiments [24].

Magnetic transition metals Cr and Fe are the exceptions. In Fe, a ⟨110⟩ dumbbell is the most stable configuration of an SIA defect [29–31]. Fu *et al.* [29] showed that this explains the origin of the relatively high temperature of stage I of resistivity recovery in electron irradiated iron, which is close to 120 K [24]. For a long time, the structure of defects in Cr remained uncertain. We have found [41] that the most stable SIA configuration in Cr is a $\langle 11\xi\rangle$ dumbbell, where $\xi = 0.355$ for the AFM state and $\xi = 0.405$ for the NM state. Calculations suggest that the defect migration pathway in Cr follows a translation-rotation pattern, changing from a $\langle 11\xi\rangle$ to an adjacent $\langle \xi 11\rangle$ dumbbell configuration [41].

The elements of dipole tensors P_{ij} and relaxation volume tensors Ω_{ij} for all the defects in all the bcc metals are given in Tables VI–XXIV. We have also determined the eigenvalues $\Omega^{(i)}$ of relaxation volume tensors, and the total relaxation volumes of defects $\Omega_{\rm rel}$ that are required as input for finite element calculations of macroscopic stresses and strains [42]. The eigenvectors of Ω_{ij} are given in Table XXV. Using these parameters, one can evaluate the strength of elastic interaction between points defects, and between a point defect and any strain field in a material. The quantities given in Tables VI–XXV relate parameters of defects, derived from simulations performed on the electronic scale, to continuum elasticity. In general, it is necessary to define three parameters, namely the eigenvalues of tensors P_{ij} or Ω_{ij}, to fully characterize the elastic field of a point defect. The eigenvectors reflect the symmetry of a particular configuration of a defect. They remain the same for the same defect configuration, whereas the eigenvalues vary from one material to another.

TABLE VI. Elements of the dipole tensor P_{ij} (in eV units), the relaxation volume tensor Ω_{ij} (in Å^3 units), eigenvalues of the relaxation volume tensor $\Omega^{(i)}$ (in Å^3 units), and the relaxation volume of the defect $\Omega_{\rm rel}$ (in atomic volume units Ω_0) computed for Li.

Li	P_{11}	P_{22}	P_{33}	P_{12}	P_{23}	P_{31}	Ω_{11}	Ω_{22}	Ω_{33}	Ω_{12}	Ω_{23}	Ω_{31}	$\Omega^{(1)}$	$\Omega^{(2)}$	$\Omega^{(3)}$	$\Omega_{\rm rel}$
⟨111⟩d	2.071	2.071	2.071	0.796	0.796	0.796	7.930	7.930	7.930	5.577	5.577	5.577	2.353	2.353	19.084	1.175
⟨111⟩c	2.063	2.063	2.063	0.761	0.761	0.761	7.899	7.899	7.899	5.334	5.334	5.334	2.566	2.566	18.567	1.171
⟨110⟩d	2.109	2.188	2.188	0.000	0.727	0.000	6.936	8.947	8.947	0.000	5.096	0.000	6.936	3.851	14.043	1.227
Tetra	2.196	2.160	2.160	0.000	0.000	0.000	8.923	8.011	8.011	0.000	0.000	0.000	8.923	8.011	8.011	1.232
⟨100⟩d	2.764	1.911	1.911	0.000	0.000	0.000	22.893	1.164	1.164	0.000	0.000	0.000	22.893	1.164	1.164	1.246
Octa	1.898	1.898	2.754	0.000	0.000	0.000	1.094	1.094	22.892	0.000	0.000	0.000	1.094	1.094	22.892	1.239
Vac	−0.937	−0.937	−0.937	0.000	0.000	0.000	−3.589	−3.589	−3.589	0.000	0.000	0.000	−3.589	−3.589	−3.589	−0.532

TABLE VII. Elements of the dipole tensor P_{ij} (in eV units), the relaxation volume tensor Ω_{ij} (in Å^3 units), eigenvalues of the relaxation volume tensor $\Omega^{(i)}$ (in Å^3 units), and the relaxation volume of the defect Ω_{rel} (in atomic volume units Ω_0) computed for Na.

Na	P_{11}	P_{22}	P_{33}	P_{12}	P_{23}	P_{31}	Ω_{11}	Ω_{22}	Ω_{33}	Ω_{12}	Ω_{23}	Ω_{31}	$\Omega^{(1)}$	$\Omega^{(2)}$	$\Omega^{(3)}$	Ω_{rel}
⟨111⟩d	2.468	2.468	2.468	0.889	0.889	0.889	16.326	16.326	16.326	11.946	11.946	11.946	4.380	4.380	40.219	1.326
⟨111⟩c	2.461	2.461	2.461	0.882	0.882	0.882	16.279	16.279	16.279	11.851	11.851	11.851	4.428	4.428	39.982	1.322
⟨110⟩d	2.575	2.478	2.478	0.000	0.738	0.000	22.068	13.871	13.871	0.000	9.924	0.000	22.068	3.947	23.794	1.348
Tetra	2.583	2.559	2.559	0.000	0.000	0.000	18.345	16.292	16.292	0.000	0.000	0.000	18.345	16.292	16.292	1.379
⟨100⟩d	3.160	2.299	2.299	0.000	0.000	0.000	65.698	−7.190	−7.190	0.000	0.000	0.000	65.698	−7.190	−7.190	1.389
Octa	2.389	2.389	3.127	0.000	0.000	0.000	−3.403	−3.403	59.092	0.000	0.000	0.000	−3.403	−3.403	59.092	1.416
Vac	−0.824	−0.824	−0.824	0.000	0.000	0.000	−5.451	−5.451	−5.451	0.000	0.000	0.000	−5.451	−5.451	−5.451	−0.443

TABLE VIII. Elements of the dipole tensor P_{ij} (in eV units), the relaxation volume tensor Ω_{ij} (in Å^3 units), eigenvalues of the relaxation volume tensor $\Omega^{(i)}$ (in Å^3 units), and the relaxation volume of the defect Ω_{rel} (in atomic volume units Ω_0) computed for K.

K	P_{11}	P_{22}	P_{33}	P_{12}	P_{23}	P_{31}	Ω_{11}	Ω_{22}	Ω_{33}	Ω_{12}	Ω_{23}	Ω_{31}	$\Omega^{(1)}$	$\Omega^{(2)}$	$\Omega^{(3)}$	Ω_{rel}
⟨111⟩d	2.260	2.260	2.260	0.793	0.793	0.793	33.581	33.581	33.581	23.572	23.572	23.572	10.009	10.009	80.725	1.368
⟨111⟩c	2.272	2.272	2.272	0.760	0.760	0.760	33.761	33.761	33.761	22.588	22.588	22.588	11.174	11.174	78.937	1.376
⟨110⟩d	2.316	2.293	2.293	0.000	0.743	0.000	39.646	31.461	31.461	0.000	22.085	0.000	39.646	9.376	53.546	1.393
Tetra	2.347	2.356	2.356	0.000	0.000	0.000	32.914	35.995	35.995	0.000	0.000	0.000	32.914	35.995	35.995	1.425
⟨100⟩d	2.875	2.144	2.144	0.000	0.000	0.000	201.895	−47.715	−47.715	0.000	0.000	0.000	201.895	−47.715	−47.715	1.446
Octa	2.167	2.167	2.846	0.000	0.000	0.000	−41.774	−41.774	190.251	0.000	0.000	0.000	−41.774	−41.774	190.251	1.449
Vac	−0.656	−0.656	−0.656	0.000	0.000	0.000	−9.744	−9.744	−9.744	0.000	0.000	0.000	−9.744	−9.744	−9.744	−0.397

TABLE IX. Elements of the dipole tensor P_{ij} (in eV units), the relaxation volume tensor Ω_{ij} (in Å^3 units), eigenvalues of the relaxation volume tensor $\Omega^{(i)}$ (in Å^3 units), and the relaxation volume of the defect Ω_{rel} (in atomic volume units Ω_0) computed for Rb.

Rb	P_{11}	P_{22}	P_{33}	P_{12}	P_{23}	P_{31}	Ω_{11}	Ω_{22}	Ω_{33}	Ω_{12}	Ω_{23}	Ω_{31}	$\Omega^{(1)}$	$\Omega^{(2)}$	$\Omega^{(3)}$	Ω_{rel}
⟨111⟩d	2.232	2.232	2.232	0.774	0.774	0.774	42.696	42.696	42.696	31.146	31.146	31.146	11.550	11.550	104.987	1.409
⟨111⟩c	2.235	2.235	2.235	0.782	0.782	0.782	42.745	42.745	42.745	31.448	31.448	31.448	11.297	11.297	105.641	1.410
⟨110⟩d	2.244	2.274	2.274	0.000	0.794	0.000	35.517	47.187	47.187	0.000	31.965	0.000	35.517	15.222	79.151	1.429
Tetra	2.248	2.354	2.354	0.000	0.000	0.000	17.093	57.968	57.968	0.000	0.000	0.000	17.093	57.968	57.968	1.463
⟨100⟩d	2.826	2.146	2.146	0.000	0.000	0.000	221.461	−42.670	−42.670	0.000	0.000	0.000	221.461	−42.670	−42.670	1.497
Octa	2.148	2.148	2.824	0.000	0.000	0.000	−42.227	−42.227	220.622	0.000	0.000	0.000	−42.227	−42.227	220.622	1.498
Vac	−0.625	−0.625	−0.625	0.000	0.000	0.000	−11.945	−11.945	−11.945	0.000	0.000	0.000	−11.945	−11.945	−11.945	−0.394

TABLE X. Elements of the dipole tensor P_{ij} (in eV units), the relaxation volume tensor Ω_{ij} (in Å^3 units), eigenvalues of the relaxation volume tensor $\Omega^{(i)}$ (in Å^3 units), and the relaxation volume of the defect Ω_{rel} (in atomic volume units Ω_0) computed for Cs.

Cs	P_{11}	P_{22}	P_{33}	P_{12}	P_{23}	P_{31}	Ω_{11}	Ω_{22}	Ω_{33}	Ω_{12}	Ω_{23}	Ω_{31}	$\Omega^{(1)}$	$\Omega^{(2)}$	$\Omega^{(3)}$	Ω_{rel}
⟨111⟩d	2.066	2.066	2.066	0.722	0.722	0.722	56.556	56.556	56.556	41.921	41.921	41.921	14.635	14.635	140.399	1.453
⟨111⟩c	2.066	2.066	2.066	0.725	0.725	0.725	56.572	56.572	56.572	42.084	42.084	42.084	14.488	14.488	140.740	1.454
⟨110⟩d	2.072	2.057	2.057	0.000	0.698	0.000	61.527	53.917	53.917	0.000	40.547	0.000	61.527	13.371	94.464	1.451
Tetra	2.083	2.151	2.151	0.000	0.000	0.000	34.847	69.993	69.993	0.000	0.000	0.000	34.847	69.993	69.993	1.498
⟨100⟩d	2.656	1.971	1.971	0.000	0.000	0.000	294.306	−56.839	−56.839	0.000	0.000	0.000	294.306	−56.839	−56.839	1.547
Octa	2.002	2.002	2.616	0.000	0.000	0.000	−44.451	−44.451	270.159	0.000	0.000	0.000	−44.451	−44.451	270.159	1.553
Vac	−0.501	−0.501	−0.501	0.000	0.000	0.000	−13.726	−13.726	−13.726	0.000	0.000	0.000	−13.726	−13.726	−13.726	−0.353

TABLE XI. Elements of the dipole tensor P_{ij} (in eV units), the relaxation volume tensor Ω_{ij} (in Å^3 units), eigenvalues of the relaxation volume tensor $\Omega^{(i)}$ (in Å^3 units), and the relaxation volume of the defect Ω_{rel} (in atomic volume units Ω_0) computed for Ba.

Ba	P_{11}	P_{22}	P_{33}	P_{12}	P_{23}	P_{31}	Ω_{11}	Ω_{22}	Ω_{33}	Ω_{12}	Ω_{23}	Ω_{31}	$\Omega^{(1)}$	$\Omega^{(2)}$	$\Omega^{(3)}$	Ω_{rel}
⟨111⟩d	4.098	4.098	4.098	2.226	2.226	2.226	24.611	24.611	24.611	17.171	17.171	17.171	7.440	7.440	58.953	1.162
⟨111⟩c	4.083	4.083	4.083	2.260	2.260	2.260	24.519	24.519	24.519	17.432	17.432	17.432	7.087	7.087	59.382	1.157
⟨110⟩d	4.061	3.822	3.822	0.000	2.176	0.000	28.805	20.742	20.742	0.000	16.786	0.000	28.805	3.956	37.527	1.106
Tetra	3.064	3.843	3.843	0.000	0.000	0.000	3.980	30.286	30.286	0.000	0.000	0.000	3.980	30.286	30.286	1.016
⟨100⟩d	4.396	2.872	2.872	0.000	0.000	0.000	54.604	3.143	3.143	0.000	0.000	0.000	54.604	3.143	3.143	0.958
Octa	2.706	2.706	4.165	0.000	0.000	0.000	2.750	2.750	52.014	0.000	0.000	0.000	2.750	2.750	52.014	0.905
Vac	−1.208	−1.208	−1.208	0.000	0.000	0.000	−7.256	−7.256	−7.256	0.000	0.000	0.000	−7.256	−7.256	−7.256	−0.343

TABLE XII. Elements of the dipole tensor P_{ij} (in eV units), the relaxation volume tensor Ω_{ij} (in Å^3 units), eigenvalues of the relaxation volume tensor $\Omega^{(i)}$ (in Å^3 units), and the relaxation volume of the defect $\Omega_{\rm rel}$ (in atomic volume units Ω_0) computed for V.

V	P_{11}	P_{22}	P_{33}	P_{12}	P_{23}	P_{31}	Ω_{11}	Ω_{22}	Ω_{33}	Ω_{12}	Ω_{23}	Ω_{31}	$\Omega^{(1)}$	$\Omega^{(2)}$	$\Omega^{(3)}$	$\Omega_{\rm rel}$
⟨111⟩d	23.140	23.140	23.140	−0.029	−0.029	−0.029	6.578	6.578	6.578	−0.086	−0.086	−0.086	6.664	6.664	6.406	1.472
⟨111⟩c	23.143	23.143	23.143	−0.081	−0.081	−0.081	6.579	6.579	6.579	−0.244	−0.244	−0.244	6.822	6.822	6.092	1.473
⟨110⟩d	19.264	24.929	24.929	0.000	−0.003	0.000	2.152	8.748	8.748	0.000	−0.009	0.000	2.152	8.757	8.739	1.466
Tetra	24.501	22.993	22.993	0.000	0.000	0.000	7.850	6.093	6.093	0.000	0.000	0.000	7.850	6.093	6.093	1.495
⟨100⟩d	26.444	22.815	22.815	0.000	0.000	0.000	9.647	5.421	5.421	0.000	0.000	0.000	9.647	5.421	5.421	1.529
Octa	22.761	22.761	26.618	0.000	0.000	0.000	5.338	5.338	9.830	0.000	0.000	0.000	5.338	5.338	9.830	1.530
Vac	−5.515	−5.515	−5.515	0.000	0.000	0.000	−1.568	−1.568	−1.568	0.000	0.000	0.000	−1.568	−1.568	−1.568	−0.351

TABLE XIII. Elements of the dipole tensor P_{ij} (in eV units), the relaxation volume tensor Ω_{ij} (in Å^3 units), eigenvalues of the relaxation volume tensor $\Omega^{(i)}$ (in Å^3 units), and the relaxation volume of the defect $\Omega_{\rm rel}$ (in atomic volume units Ω_0) computed for V using the AM05 exchange-correlation functional.

V	P_{11}	P_{22}	P_{33}	P_{12}	P_{23}	P_{31}	Ω_{11}	Ω_{22}	Ω_{33}	Ω_{12}	Ω_{23}	Ω_{31}	$\Omega^{(1)}$	$\Omega^{(2)}$	$\Omega^{(3)}$	$\Omega_{\rm rel}$
⟨111⟩d	21.261	21.261	21.261	−0.022	−0.022	−0.022	5.636	5.636	5.636	−0.055	−0.055	−0.055	5.691	5.691	5.525	1.310
⟨111⟩c	21.222	21.222	21.222	−0.078	−0.078	−0.078	5.625	5.625	5.625	−0.201	−0.201	−0.201	5.826	5.826	5.224	1.307
⟨110⟩d	17.189	23.148	23.148	0.000	0.066	0.000	1.645	7.591	7.591	0.000	0.169	0.000	1.645	7.423	7.760	1.304
Tetra	22.560	20.897	20.897	0.000	0.000	0.000	6.792	5.133	5.133	0.000	0.000	0.000	6.792	5.133	5.133	1.322
⟨100⟩d	24.699	20.707	20.707	0.000	0.000	0.000	8.497	4.514	4.514	0.000	0.000	0.000	8.497	4.514	4.514	1.358
Octa	20.695	20.695	24.907	0.000	0.000	0.000	4.457	4.457	8.660	0.000	0.000	0.000	4.457	4.457	8.660	1.361
Vac	−7.791	−7.791	−7.791	0.000	0.000	0.000	−2.065	−2.065	−2.065	0.000	0.000	0.000	−2.065	−2.065	−2.065	−0.480

TABLE XIV. Elements of the dipole tensor P_{ij} (in eV units), the relaxation volume tensor Ω_{ij} (in Å^3 units), eigenvalues of the relaxation volume tensor $\Omega^{(i)}$ (in Å^3 units), and the relaxation volume of the defect $\Omega_{\rm rel}$ (in atomic volume units Ω_0) computed for Nb.

Nb	P_{11}	P_{22}	P_{33}	P_{12}	P_{23}	P_{31}	Ω_{11}	Ω_{22}	Ω_{33}	Ω_{12}	Ω_{23}	Ω_{31}	$\Omega^{(1)}$	$\Omega^{(2)}$	$\Omega^{(3)}$	$\Omega_{\rm rel}$
⟨111⟩d	30.772	30.772	30.772	2.994	2.994	2.994	9.495	9.495	9.495	12.324	12.324	12.324	−2.829	−2.829	34.143	1.554
⟨111⟩c	30.758	30.758	30.758	2.959	2.959	2.959	9.491	9.491	9.491	12.181	12.181	12.181	−2.690	−2.690	33.852	1.553
⟨110⟩d	29.739	30.813	30.813	0.000	1.443	0.000	8.387	9.902	9.902	0.000	5.938	0.000	8.387	3.964	15.841	1.538
Tetra	31.916	30.687	30.687	0.000	0.000	0.000	10.752	9.017	9.017	0.000	0.000	0.000	10.752	9.017	9.017	1.571
⟨100⟩d	37.069	30.512	30.512	0.000	0.000	0.000	16.259	7.005	7.005	0.000	0.000	0.000	16.259	7.005	7.005	1.651
Octa	31.153	31.153	35.689	0.000	0.000	0.000	7.945	7.945	14.347	0.000	0.000	0.000	7.945	7.945	14.347	1.650
Vac	−8.805	−8.805	−8.805	0.000	0.000	0.000	−2.717	−2.717	−2.717	0.000	0.000	0.000	−2.717	−2.717	−2.717	−0.445

TABLE XV. Elements of the dipole tensor P_{ij} (in eV units), the relaxation volume tensor Ω_{ij} (in Å^3 units), eigenvalues of the relaxation volume tensor $\Omega^{(i)}$ (in Å^3 units), and the relaxation volume of the defect $\Omega_{\rm rel}$ (in atomic volume units Ω_0) computed for Nb using the AM05 exchange-correlation functional.

Nb	P_{11}	P_{22}	P_{33}	P_{12}	P_{23}	P_{31}	Ω_{11}	Ω_{22}	Ω_{33}	Ω_{12}	Ω_{23}	Ω_{31}	$\Omega^{(1)}$	$\Omega^{(2)}$	$\Omega^{(3)}$	$\Omega_{\rm rel}$
⟨111⟩d	31.698	31.698	31.698	3.004	3.004	3.004	9.074	9.074	9.074	10.191	10.191	10.191	−1.117	−1.117	29.456	1.540
⟨111⟩c	31.681	31.681	31.681	2.964	2.964	2.964	9.070	9.070	9.070	10.054	10.054	10.054	−0.985	−0.985	29.178	1.539
⟨110⟩d	30.455	31.552	31.552	0.000	1.256	0.000	8.030	9.377	9.377	0.000	4.261	0.000	8.030	5.116	13.638	1.515
Tetra	32.739	31.201	31.201	0.000	0.000	0.000	10.338	8.450	8.450	0.000	0.000	0.000	10.338	8.450	8.450	1.541
⟨100⟩d	37.685	31.168	31.168	0.000	0.000	0.000	14.879	6.878	6.878	0.000	0.000	0.000	14.879	6.878	6.878	1.620
Octa	31.823	31.823	36.123	0.000	0.000	0.000	7.761	7.761	13.040	0.000	0.000	0.000	7.761	7.761	13.040	1.616
Vac	−9.175	−9.175	−9.175	0.000	0.000	0.000	−2.627	−2.627	−2.627	0.000	0.000	0.000	−2.627	−2.627	−2.627	−0.446

TABLE XVI. Elements of the dipole tensor P_{ij} (in eV units), the relaxation volume tensor Ω_{ij} (in Å^3 units), eigenvalues of the relaxation volume tensor $\Omega^{(i)}$ (in Å^3 units), and the relaxation volume of the defect $\Omega_{\rm rel}$ (in atomic volume units Ω_0) computed for Mo.

Mo	P_{11}	P_{22}	P_{33}	P_{12}	P_{23}	P_{31}	Ω_{11}	Ω_{22}	Ω_{33}	Ω_{12}	Ω_{23}	Ω_{31}	$\Omega^{(1)}$	$\Omega^{(2)}$	$\Omega^{(3)}$	$\Omega_{\rm rel}$
⟨111⟩d	39.601	39.601	39.601	7.609	7.609	7.609	8.087	8.087	8.087	6.113	6.113	6.113	1.975	1.975	20.313	1.538
⟨111⟩c	39.597	39.597	39.597	7.599	7.599	7.599	8.087	8.087	8.087	6.105	6.105	6.105	1.982	1.982	20.297	1.538
⟨110⟩d	42.470	39.944	39.944	0.000	6.757	0.000	9.196	7.896	7.896	0.000	5.429	0.000	9.196	2.468	13.325	1.584
Tetra	37.531	43.685	43.685	0.000	0.000	0.000	6.391	9.558	9.558	0.000	0.000	0.000	6.391	9.558	9.558	1.617
⟨100⟩d	48.989	40.370	40.370	0.000	0.000	0.000	11.788	7.353	7.353	0.000	0.000	0.000	11.788	7.353	7.353	1.680
Octa	39.601	39.601	50.174	0.000	0.000	0.000	6.994	6.994	12.435	0.000	0.000	0.000	6.994	6.994	12.435	1.675
Vac	−9.576	−9.576	−9.576	0.000	0.000	0.000	−1.956	−1.956	−1.956	0.000	0.000	0.000	−1.956	−1.956	−1.956	−0.372

TABLE XVII. Elements of the dipole tensor P_{ij} (in eV units), the relaxation volume tensor Ω_{ij} (in Å^3 units), eigenvalues of the relaxation volume tensor $\Omega^{(i)}$ (in Å^3 units), and the relaxation volume of the defect $\Omega_{\rm rel}$ (in atomic volume units Ω_0) computed for Mo using the AM05 exchange-correlation functional.

Mo	P_{11}	P_{22}	P_{33}	P_{12}	P_{23}	P_{31}	Ω_{11}	Ω_{22}	Ω_{33}	Ω_{12}	Ω_{23}	Ω_{31}	$\Omega^{(1)}$	$\Omega^{(2)}$	$\Omega^{(3)}$	$\Omega_{\rm rel}$
⟨111⟩d	40.358	40.358	40.358	7.777	7.777	7.777	7.554	7.554	7.554	5.767	5.767	5.767	1.787	1.787	19.088	1.487
⟨111⟩c	40.352	40.352	40.352	7.771	7.771	7.771	7.553	7.553	7.553	5.762	5.762	5.762	1.791	1.791	19.076	1.487
⟨110⟩d	43.230	40.736	40.736	0.000	7.015	0.000	8.588	7.377	7.377	0.000	5.201	0.000	8.588	2.176	12.578	1.532
Tetra	38.319	44.282	44.282	0.000	0.000	0.000	5.987	8.881	8.881	0.000	0.000	0.000	5.987	8.881	8.881	1.558
⟨100⟩d	49.636	41.001	41.001	0.000	0.000	0.000	11.007	6.817	6.817	0.000	0.000	0.000	11.007	6.817	6.817	1.617
Octa	40.239	40.239	50.956	0.000	0.000	0.000	6.467	6.467	11.668	0.000	0.000	0.000	6.467	6.467	11.668	1.614
Vac	−10.442	−10.442	−10.442	0.000	0.000	0.000	−1.955	−1.955	−1.955	0.000	0.000	0.000	−1.955	−1.955	−1.955	−0.385

TABLE XVIII. Elements of the dipole tensor P_{ij} (in eV units), the relaxation volume tensor Ω_{ij} (in Å^3 units), eigenvalues of the relaxation volume tensor $\Omega^{(i)}$ (in Å^3 units), and the relaxation volume of the defect $\Omega_{\rm rel}$ (in atomic volume units Ω_0) computed for Ta.

Ta	P_{11}	P_{22}	P_{33}	P_{12}	P_{23}	P_{31}	Ω_{11}	Ω_{22}	Ω_{33}	Ω_{12}	Ω_{23}	Ω_{31}	$\Omega^{(1)}$	$\Omega^{(2)}$	$\Omega^{(3)}$	$\Omega_{\rm rel}$
⟨111⟩d	34.153	34.153	34.153	6.518	6.518	6.518	9.290	9.290	9.290	6.803	6.803	6.803	2.487	2.487	22.896	1.524
⟨111⟩c	34.155	34.155	34.155	6.493	6.493	6.493	9.291	9.291	9.291	6.777	6.777	6.777	2.514	2.514	22.845	1.524
⟨110⟩d	31.793	34.491	34.491	0.000	5.451	0.000	6.391	10.511	10.511	0.000	5.690	0.000	6.391	4.821	16.200	1.499
Tetra	34.739	34.989	34.989	0.000	0.000	0.000	9.241	9.622	9.622	0.000	0.000	0.000	9.241	9.622	9.622	1.557
⟨100⟩d	42.520	33.765	33.765	0.000	0.000	0.000	18.891	5.522	5.522	0.000	0.000	0.000	18.891	5.522	5.522	1.636
Octa	34.134	34.134	42.378	0.000	0.000	0.000	5.836	5.836	18.425	0.000	0.000	0.000	5.836	5.836	18.425	1.645
Vac	−10.119	−10.119	−10.119	0.000	0.000	0.000	−2.753	−2.753	−2.753	0.000	0.000	0.000	−2.753	−2.753	−2.753	−0.451

TABLE XIX. Elements of the dipole tensor P_{ij} (in eV units), the relaxation volume tensor Ω_{ij} (in Å^3 units), eigenvalues of the relaxation volume tensor $\Omega^{(i)}$ (in Å^3 units), and the relaxation volume of the defect $\Omega_{\rm rel}$ (in atomic volume units Ω_0) computed for Ta using the AM05 exchange-correlation functional.

Ta	P_{11}	P_{22}	P_{33}	P_{12}	P_{23}	P_{31}	Ω_{11}	Ω_{22}	Ω_{33}	Ω_{12}	Ω_{23}	Ω_{31}	$\Omega^{(1)}$	$\Omega^{(2)}$	$\Omega^{(3)}$	$\Omega_{\rm rel}$
⟨111⟩d	34.672	34.672	34.672	6.634	6.634	6.634	8.820	8.820	8.820	6.475	6.475	6.475	2.346	2.346	21.770	1.502
⟨111⟩c	34.669	34.669	34.669	6.617	6.617	6.617	8.820	8.820	8.820	6.458	6.458	6.458	2.361	2.361	21.736	1.502
⟨110⟩d	32.291	34.687	34.687	0.000	5.389	0.000	6.578	9.642	9.642	0.000	5.259	0.000	6.578	4.383	14.902	1.468
Tetra	34.868	35.361	35.361	0.000	0.000	0.000	8.533	9.164	9.164	0.000	0.000	0.000	8.533	9.164	9.164	1.525
⟨100⟩d	43.261	33.980	33.980	0.000	0.000	0.000	17.345	5.475	5.475	0.000	0.000	0.000	17.345	5.475	5.475	1.606
Octa	34.482	34.482	43.268	0.000	0.000	0.000	5.771	5.771	17.009	0.000	0.000	0.000	5.771	5.771	17.009	1.621
Vac	−10.703	−10.703	−10.703	0.000	0.000	0.000	−2.723	−2.723	−2.723	0.000	0.000	0.000	−2.723	−2.723	−2.723	−0.464

TABLE XX. Elements of the dipole tensor P_{ij} (in eV units), the relaxation volume tensor Ω_{ij} (in Å^3 units), eigenvalues of the relaxation volume tensor $\Omega^{(i)}$ (in Å^3 units), and the relaxation volume of the defect $\Omega_{\rm rel}$ (in atomic volume units Ω_0) computed for W.

W	P_{11}	P_{22}	P_{33}	P_{12}	P_{23}	P_{31}	Ω_{11}	Ω_{22}	Ω_{33}	Ω_{12}	Ω_{23}	Ω_{31}	$\Omega^{(1)}$	$\Omega^{(2)}$	$\Omega^{(3)}$	$\Omega_{\rm rel}$
⟨111⟩d	52.754	52.754	52.754	13.128	13.128	13.128	9.209	9.209	9.209	7.402	7.402	7.402	1.808	1.808	24.012	1.712
⟨111⟩c	52.745	52.745	52.745	13.151	13.151	13.151	9.207	9.207	9.207	7.414	7.414	7.414	1.793	1.793	24.036	1.711
⟨110⟩d	56.960	52.557	52.557	0.000	11.277	0.000	10.908	8.693	8.693	0.000	6.358	0.000	10.908	2.335	15.050	1.753
Tetra	47.359	59.114	59.114	0.000	0.000	0.000	5.693	11.606	11.606	0.000	0.000	0.000	5.693	11.606	11.606	1.791
⟨100⟩d	65.920	53.379	53.379	0.000	0.000	0.000	14.254	7.945	7.945	0.000	0.000	0.000	14.254	7.945	7.945	1.868
Octa	52.741	52.741	67.209	0.000	0.000	0.000	7.623	7.623	14.901	0.000	0.000	0.000	7.623	7.623	14.901	1.868
Vac	−9.984	−9.984	−9.984	0.000	0.000	0.000	−1.743	−1.743	−1.743	0.000	0.000	0.000	−1.743	−1.743	−1.743	−0.324

TABLE XXI. Elements of elastic dipole tensor P_{ij} (in eV units), the relaxation volume tensor Ω_{ij} (in Å^3 units), eigenvalues of the relaxation volume tensor $\Omega^{(i)}$ (in Å^3 units), and the relaxation volume of the defect $\Omega_{\rm rel}$ (in atomic volume Ω_0 units) computed for W. Simulation cells containing defects were relaxed to the stress-free condition.

W	P_{11}	P_{22}	P_{33}	P_{12}	P_{23}	P_{31}	Ω_{11}	Ω_{22}	Ω_{33}	Ω_{12}	Ω_{23}	Ω_{31}	$\Omega^{(1)}$	$\Omega^{(2)}$	$\Omega^{(3)}$	$\Omega_{\rm rel}$
⟨111⟩d	52.340	52.340	52.340	12.854	12.854	12.854	9.137	9.137	9.137	7.247	7.247	7.247	1.890	1.890	23.630	1.698
⟨111⟩c	52.325	52.325	52.325	12.897	12.897	12.897	9.134	9.134	9.134	7.271	7.271	7.271	1.863	1.863	23.676	1.698
⟨110⟩d	56.199	52.115	52.115	0.000	11.361	0.000	10.705	8.650	8.650	0.000	6.405	0.000	10.705	2.245	15.055	1.735
Tetra	45.940	59.120	59.120	0.000	0.000	0.000	5.133	11.764	11.764	0.000	0.000	0.000	5.133	11.764	11.764	1.776
⟨100⟩d	65.719	52.807	52.807	0.000	0.000	0.000	14.300	7.805	7.805	0.000	0.000	0.000	14.300	7.805	7.805	1.853
Octa	51.994	51.994	67.258	0.000	0.000	0.000	7.405	7.405	15.084	0.000	0.000	0.000	7.405	7.405	15.084	1.852
Vac	−10.112	−10.112	−10.112	0.000	0.000	0.000	−1.765	−1.765	−1.765	0.000	0.000	0.000	−1.765	−1.765	−1.765	−0.328

TABLE XXII. Elements of the dipole tensor P_{ij} (in eV units), the relaxation volume tensor Ω_{ij} (in Å^3 units), eigenvalues of the relaxation volume tensor $\Omega^{(i)}$ (in Å^3 units), and the relaxation volume of the defect $\Omega_{\rm rel}$ (in atomic volume units Ω_0) computed for W using the AM05 exchange-correlation functional.

W	P_{11}	P_{22}	P_{33}	P_{12}	P_{23}	P_{31}	Ω_{11}	Ω_{22}	Ω_{33}	Ω_{12}	Ω_{23}	Ω_{31}	$\Omega^{(1)}$	$\Omega^{(2)}$	$\Omega^{(3)}$	$\Omega_{\rm rel}$
⟨111⟩d	53.843	53.843	53.843	13.218	13.218	13.218	8.689	8.689	8.689	6.738	6.738	6.738	1.952	1.952	22.164	1.669
⟨111⟩c	53.843	53.843	53.843	13.243	13.243	13.243	8.689	8.689	8.689	6.750	6.750	6.750	1.939	1.939	22.190	1.669
⟨110⟩d	57.374	53.705	53.705	0.000	11.768	0.000	9.958	8.318	8.318	0.000	5.999	0.000	9.958	2.319	14.316	1.703
Tetra	48.127	59.932	59.932	0.000	0.000	0.000	5.517	10.797	10.797	0.000	0.000	0.000	5.517	10.797	10.797	1.736
⟨100⟩d	66.337	53.846	53.846	0.000	0.000	0.000	13.086	7.500	7.500	0.000	0.000	0.000	13.086	7.500	7.500	1.799
Octa	53.259	53.259	68.305	0.000	0.000	0.000	7.161	7.161	13.891	0.000	0.000	0.000	7.161	7.161	13.891	1.807
Vac	−10.951	−10.951	−10.951	0.000	0.000	0.000	−1.767	−1.767	−1.767	0.000	0.000	0.000	−1.767	−1.767	−1.767	−0.340

TABLE XXIII. Elements of the dipole tensor P_{ij} (in eV units), the relaxation volume tensor Ω_{ij} (in Å^3 units), eigenvalues of the relaxation volume tensor $\Omega^{(i)}$ (in Å^3 units), and the relaxation volume of the defect $\Omega_{\rm rel}$ (in atomic volume units Ω_0) computed for Cr.

Cr	P_{11}	P_{22}	P_{33}	P_{12}	P_{23}	P_{31}	Ω_{11}	Ω_{22}	Ω_{33}	Ω_{12}	Ω_{23}	Ω_{31}	$\Omega^{(1)}$	$\Omega^{(2)}$	$\Omega^{(3)}$	$\Omega_{\rm rel}$
⟨111⟩d	18.728	18.728	18.728	4.617	4.617	4.617	5.244	5.244	5.244	3.622	3.622	3.622	1.622	1.622	12.487	1.343
⟨111⟩c	19.630	19.630	19.630	4.882	4.882	4.882	5.497	5.497	5.497	3.830	3.830	3.830	1.667	1.667	13.156	1.407
⟨110⟩d	18.955	20.530	20.530	0.000	4.790	0.000	5.166	5.820	5.820	0.000	3.757	0.000	5.166	2.062	9.577	1.434
Tetra	16.255	25.473	25.474	0.000	0.000	0.000	3.722	7.547	7.548	0.000	0.000	0.000	3.722	7.547	7.548	1.606
⟨100⟩d	29.090	19.150	19.150	0.000	0.000	0.000	9.040	4.915	4.915	0.000	0.000	0.000	9.040	4.915	4.915	1.610
Octa	17.321	17.321	32.707	0.000	0.000	0.000	4.158	4.158	10.543	0.000	0.000	0.000	4.158	4.158	10.543	1.609
Vac	−5.777	−5.777	−5.777	0.000	0.000	0.000	−1.618	−1.618	−1.618	0.000	0.000	0.000	−1.618	−1.618	−1.618	−0.414
⟨11ξ⟩d	18.389	18.389	21.882	4.040	2.058	2.058	4.987	4.987	6.436	3.168	1.614	1.614	1.819	4.856	9.734	1.400

TABLE XXIV. Elements of the dipole tensor P_{ij} (in eV units), the relaxation volume tensor Ω_{ij} (in Å^3 units), eigenvalues of the relaxation volume tensor $\Omega^{(i)}$ (in Å^3 units), and the relaxation volume of the defect $\Omega_{\rm rel}$ (in atomic volume units Ω_0) computed for Fe.

Fe	P_{11}	P_{22}	P_{33}	P_{12}	P_{23}	P_{31}	Ω_{11}	Ω_{22}	Ω_{33}	Ω_{12}	Ω_{23}	Ω_{31}	$\Omega^{(1)}$	$\Omega^{(2)}$	$\Omega^{(3)}$	$\Omega_{\rm rel}$
⟨111⟩d	23.465	23.465	23.472	5.850	5.851	5.851	6.327	6.327	6.335	4.362	4.363	4.363	1.964	1.964	15.051	1.673
⟨111⟩c	23.186	23.186	23.193	5.903	5.904	5.904	6.252	6.252	6.259	4.402	4.402	4.402	1.850	1.850	15.056	1.653
⟨110⟩d	25.832	21.143	21.150	0.000	5.122	0.000	9.777	4.294	4.302	0.000	3.819	0.000	9.777	0.475	8.122	1.620
Tetra	21.396	23.331	23.339	0.000	0.001	0.000	4.607	6.871	6.880	0.000	0.000	0.000	4.607	6.871	6.880	1.619
⟨100⟩d	32.284	22.931	22.937	0.000	0.000	0.000	14.316	3.378	3.385	0.000	0.000	0.000	14.316	3.378	3.385	1.858
Octa	23.273	23.273	31.302	0.000	0.000	0.000	3.869	3.869	13.258	0.000	0.000	0.000	3.869	3.869	13.258	1.851
Vac	−3.081	−3.081	−3.081	0.000	0.000	0.000	−0.831	−0.831	−0.831	0.000	0.000	0.000	−0.831	−0.831	−0.831	−0.220

Defects in the NM transition metals were studied using the PBE and AM05 functionals, which produce slightly different results. If we use the relaxation volume $\Omega_{\rm rel}$ of a defect as a criterion to compare the values obtained using PBE and AM05 functionals then, with the exception of vanadium, the difference is smaller than 5%. This 5% error is in fact compatible with the error margin of the linear elasticity approximation resulting from the ratio of sizes of the core of the defect and the simulation cell [7]. Using semiempirical potentials and molecular statics calculations, we found that obtaining a converged value of the dipole tensor requires using a cell containing at least a few thousand atoms [7]. For vanadium, the difference between the values computed using the two functionals is greater. At this point, it is difficult to establish what exchange-correlation functional is more suitable for quantitative simulations of elastic properties of defects in vanadium.

We have also computed elastic parameters of defects in tungsten, using zero stress simulations. Tables XX and XXI show values computed using fixed and relaxed boundary conditions. The values computed using the two different methods are comparable, and the difference between them is due to the fact that a finite value of applied strain was used when computing the elastic correction, whereas linear elasticity is valid only in the limit of infinitesimally small strain.

IV. MIGRATION OF A SELF-INTERSTITIAL ATOM DEFECT IN IRON AND CHROMIUM

The translation-rotation migration step of a ⟨110⟩ dumbbell in Fe was examined using the NEB method calculations [61,62]. Eleven images were used to represent the trajectory linking the initial and final equilibrium positions of the defect. Figure 4 shows how the energy of the defect varies when a ⟨110⟩ dumbbell migrates along its transition pathway. All the data points are corrected according to Eq. (6). The saddle point energy of 0.34 eV for migration of an SIA defect in Fe agrees with the value computed by Fu *et al.* [29].

Since Fe is FM, it is interesting to study its magnetic configuration. During defect migration, the magnetic configuration changes according to the position of the core of the ⟨110⟩ dumbbell. Changes of magnetic moments are shown in Figs. 5 and 6. At the core of the ⟨110⟩ dumbbell, magnetic moments of the two atoms are ordered antiferromagnetically with respect to the lattice. When the core migrates, one of the two core atoms replaces an adjacent atom. The magnetic configuration remains the same at the two equilibrium positions, whereas at the saddle point we observe that the magnetic moment of only one atom is antiferromagnetically ordered with respect to the surrounding lattice. Given that migration of the defect can occur at a relatively low temperature, well below the Curie temperature of iron, it would be interesting to explore whether the magnetic dynamics of atomic moments has an effect on the migration pathway. In Fig. 5, we also plot the Voronoi volume of atoms in the core of the defect. The data exhibit a positive magneto-volume correlation, i.e., a smaller value of the Voronoi volume of an

TABLE XXV. Eigenvectors corresponding to the eigenvalues of the relaxation volume tensor of various defect configurations. Eigenvectors for the relaxation volume tensor of a ⟨11ξ⟩ dumbbell are given only for Cr.

	$\mathbf{e}^{(1)}$	$\mathbf{e}^{(2)}$	$\mathbf{e}^{(3)}$
⟨111⟩d	(1 1 −2)	(−1 1 0)	(1 1 1)
⟨111⟩c	(1 1 −2)	(−1 1 0)	(1 1 1)
⟨110⟩d	(1 0 0)	(0 −1 1)	(0 1 1)
Tetra	(1 0 0)	(0 1 0)	(0 0 1)
⟨100⟩d	(1 0 0)	(0 1 0)	(0 0 1)
Octa	(1 0 0)	(0 1 0)	(0 0 1)
Vac	(1 0 0)	(0 1 0)	(0 0 1)
⟨11ξ⟩d	(−1 1 0)	(−0.4893 −0.4893 1)	(1.0218 1.0218 1)

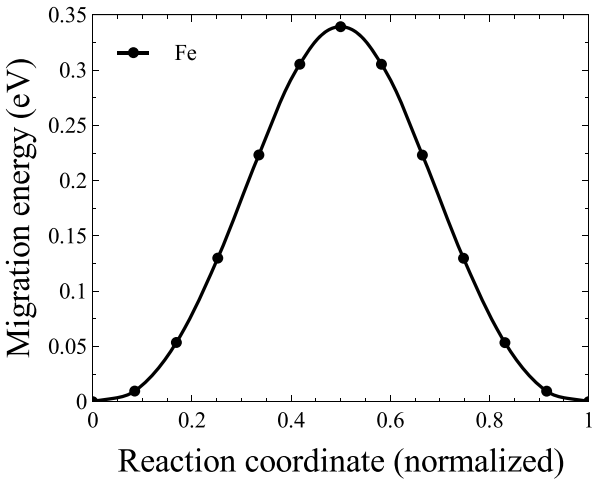

FIG. 4. Variation of energy along the migration pathway of a ⟨110⟩ dumbbell in Fe.

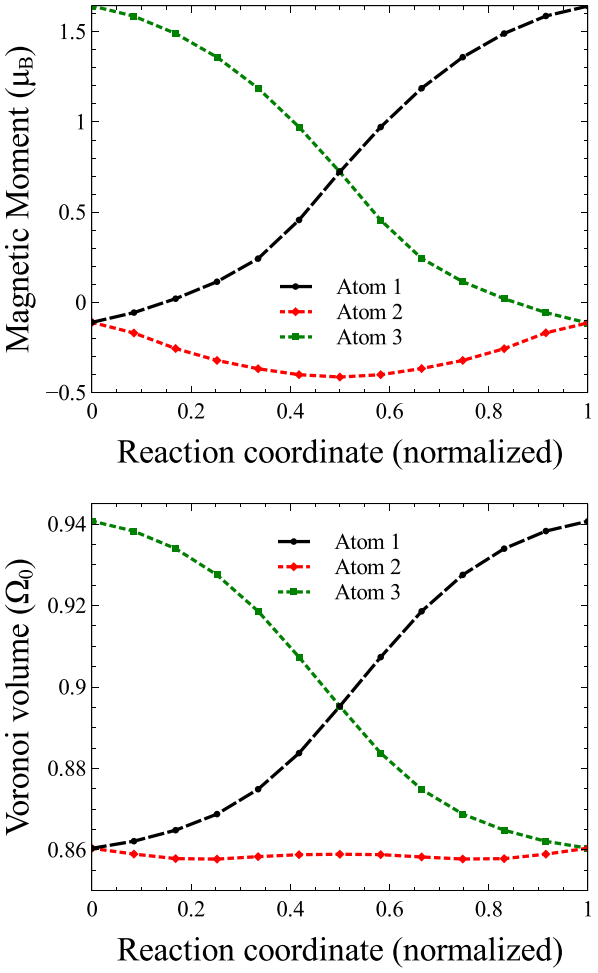

FIG. 5. Magnetic moments and the Voronoi volume of the three atoms undergoing the greatest displacement during the migration of a ⟨110⟩ dumbbell in Fe. Atoms 1 and 2 are the two atoms that are initially at the center of the SIA configuration, whereas atoms 2 and 3 form of the center of the defect at its final position.

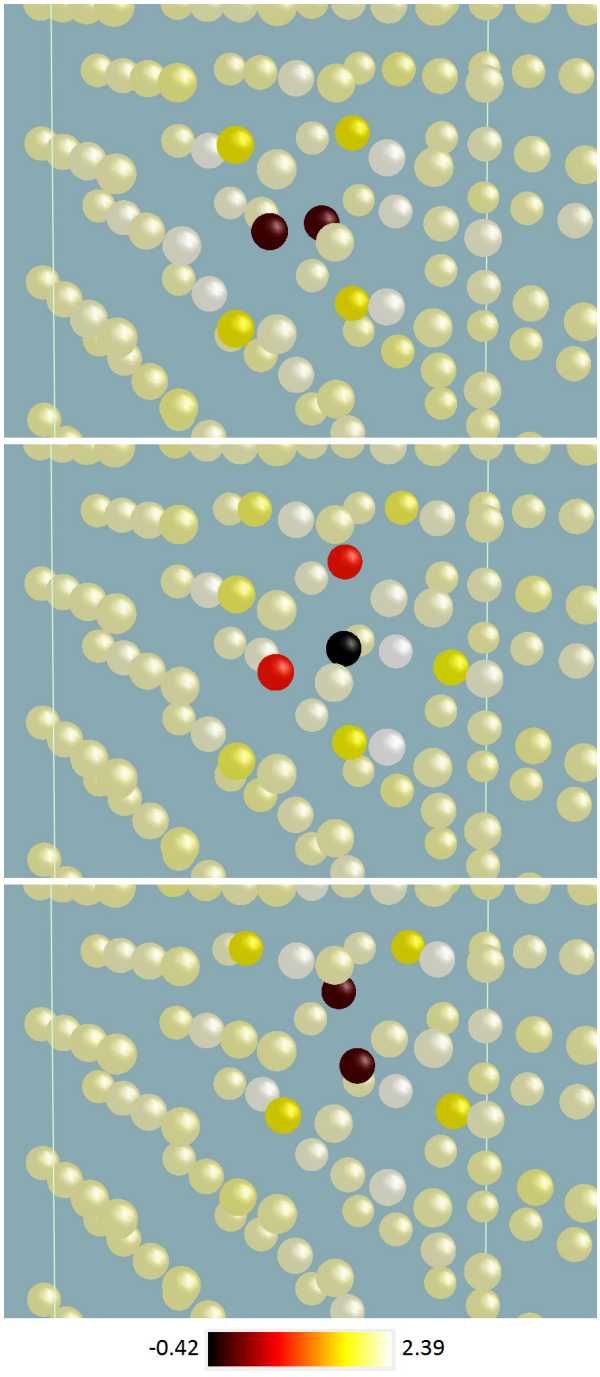

FIG. 6. Migration of a ⟨110⟩ dumbbell in Fe. Top: The initial atomic configuration; Middle: The saddle point; Bottom: The final configuration. The color of atoms refers to the magnitude of atomic magnetic moments given in Bohr magneton units μ_B.

atom is associated with a smaller atomic magnetic moment. The Voronoi volume was calculated using program Voro++ [63].

Variation of the elements of elastic dipole tensor of a ⟨110⟩ dumbbell in Fe along the defect migration pathway is illustrated in Fig. 7. The evolution of the relaxation volume tensor along the same pathway is shown in Fig. 8. The figures show that elements P_{11} and P_{33} change due to the change of orientation of the ⟨110⟩ defect from its initial position in the $x-y$ plane to its final position in the $y-z$ plane. A similar variation is observed for the off-diagonal elements of tensor P_{ij}, and for the elements of the relaxation volume tensor.

The above results pose an interesting question, related to the timescale of the process of migration, and the validity of static elastic approximation for the treatment of defect configurations along the migration pathway. The static elastic approximation remains valid if the process of migration is slow in comparison with the time required for the sound waves to propagate to the object with which a migrating defect interacts. At larger distances between any two interacting and moving defects, one expects to observe delayed elastic interaction, mediated by sound waves propagating through the material slower than the time required for a defect to complete its translation-rotation jump. Retarded time-dependent elastic interactions between dislocations have been recently explored in Refs. [74,75]. Also, thermal fluctuations contribute to the force acting between elastically interacting defects [76].

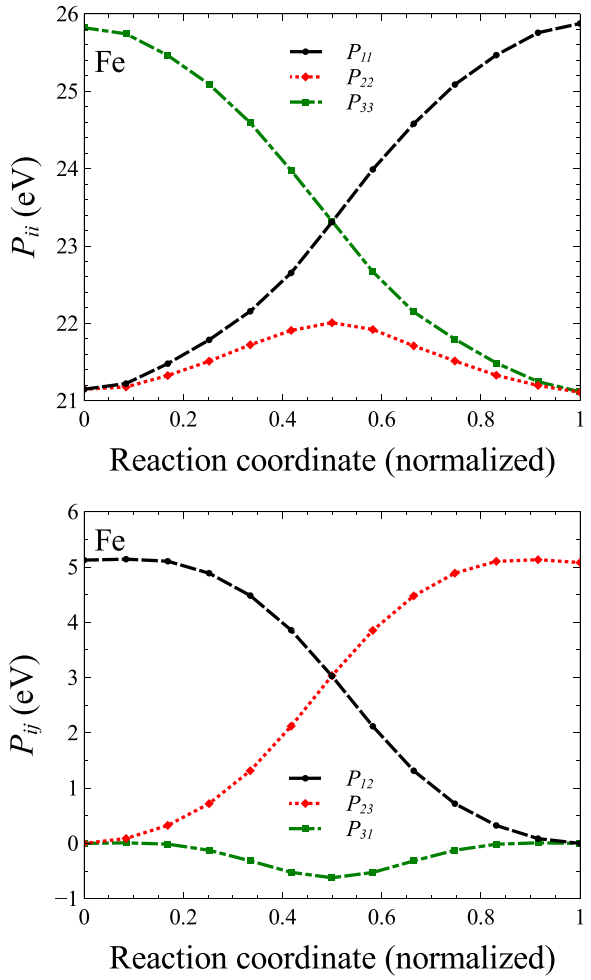

FIG. 7. Variation of elements of the dipole tensor of a ⟨110⟩ dumbbell in Fe along the defect migration pathway.

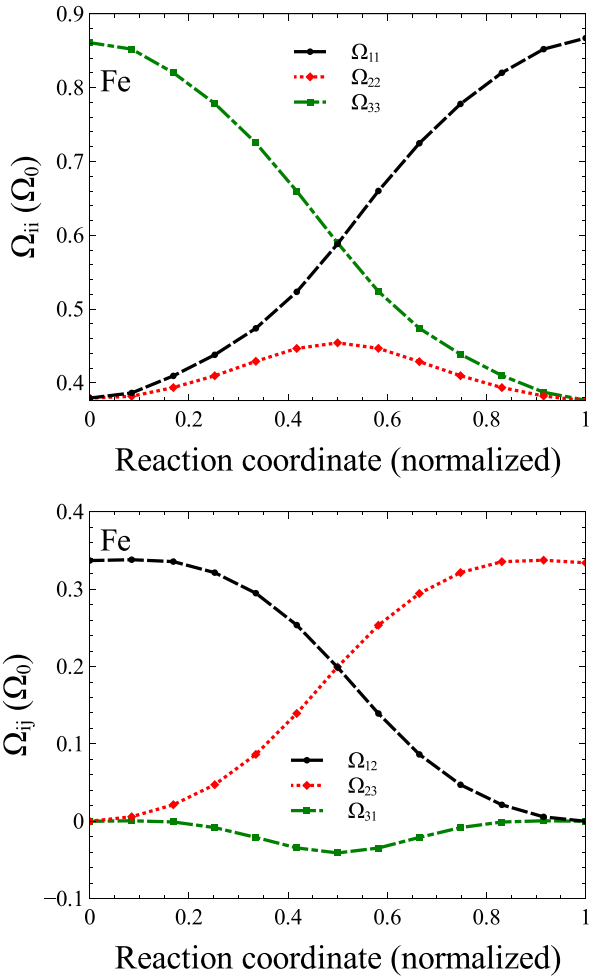

FIG. 8. Variation of the relaxation volume tensor of a ⟨110⟩ dumbbell in Fe along the defect migration pathway. The values are given in atomic volume units.

V. CONCLUSIONS

In this paper, we have investigated formation and migration energies, elastic dipole, and relaxation volume tensors of self-interstitial and vacancy defects in all the bcc metals in the periodic table. In all these metals, including metals of groups 1 and 2, the lowest energy structure of an SIA defect is universal and has the ⟨111⟩ symmetry. In FM Fe, an SIA defect adopts the ⟨110⟩ dumbbell configuration. We have also computed elastic dipole tensors and relaxation volumes of self-interstitial and vacancy defects in all the bcc metals and explored how elastic relaxation parameters evolve along the defect migration pathways.

ACKNOWLEDGMENTS

This work has been carried out within the framework of the EUROfusion Consortium and has received funding from the Euratom research and training program 2014–2018 and 2019–2020 under Grant Agreement No. 633053 and from the RCUK Energy Programme [Grant No. EP/P012450/1]. To obtain further information on the data and models underlying this paper, please contact PublicationsManager@ukaea.uk. The views and opinions expressed herein do not necessarily reflect those of the European Commission. S.L.D. also acknowledges support from the Centre for Non-Linear Studies at LANL. We also acknowledge EUROfusion for the provision of access to Marconi supercomputer facility at CINECA in Italy.

[1] W. Cai and W. D. Nix, *Imperfections in Crystalline Solids* (Cambridge University Press, Cambridge, 2016).

[2] P. H. Dederichs, C. Lehmann, H. R. Schober, A. Scholz, and R. Zeller, Lattice theory of point defects, J. Nucl. Mater. **69**, 176 (1978).

[3] W. Schilling, Self-interstitial atoms in metals, J. Nucl. Mater. **69**, 465 (1978).

[4] E. Clouet, S. Garruchet, H. Nguyen, M. Perez, and C. S. Becquart, Dislocation interaction with C in α-Fe: A comparison between atomic simulations and elasticity theory, Acta Mater. **56**, 3450 (2008).

[5] C. Varvenne, F. Bruneval, M.-C. Marinica, and E. Clouet, Point defect modeling in materials: Coupling *ab initio* and elasticity approaches, Phys. Rev. B **88**, 134102 (2013).

[6] C. Varvenne and E. Clouet, Elastic dipoles of point defects from atomistic simulations, Phys. Rev. B **96**, 224103 (2017).
[7] S. L. Dudarev and P.-W. Ma, Elastic fields, dipole tensors, and interaction between self-interstitial atom defects in bcc transition metals, Phys. Rev. Mater. **2**, 033602 (2018).
[8] S. L. Dudarev, M. R. Gilbert, K. Arakawa, H. Mori, Z. Yao, M. L. Jenkins, and P. M. Derlet, Langevin model for real-time Brownian dynamics of interacting nanodefects in irradiated metals, Phys. Rev. B **81**, 224107 (2010).
[9] G. Leibfried and N. Breuer, *Point Defects in Metals* (Springer, Berlin, 1978), p. 161
[10] D. M. Barnett, The precise evaluation of derivatives of the anisotropic elastic Green's functions, Phys. Status Solidi B **49**, 741 (1972).
[11] C. Domain and C. S. Becquart, *Ab initio* calculations of defects in Fe and dilute Fe-Cu alloys, Phys. Rev. B **65**, 024103 (2001).
[12] A. B. Sivak, V. A. Romanov, and V. M. Chernov, Diffusion of self-point defects in body-centered cubic iron crystal containing dislocations, Crystallogr. Rep. **55**, 97 (2010).
[13] M. Boleininger, T. D. Swinburne, and S. L. Dudarev, Atomistic-to-continuum description of edge dislocation core: Unification of the Peierls-Nabarro model with linear elasticity, Phys. Rev. Materials **2**, 083803 (2018).
[14] A. B. Sivak, V. M. Chernov, V. A. Romanov, and P. A. Sivak, Kinetic Monte-Carlo simulation of self-point defect diffusion in dislocation elastic fields in bcc iron and vanadium, J. Nucl. Mater. **417**, 1067 (2011).
[15] A. B. Sivak, P. A. Sivak, V. A. Romanov, and V. M. Chernov, Energetic, crystallographic and diffusion characteristics of hydrogen isotopes in iron, J. Nucl. Mater. **461**, 308 (2015).
[16] A. B. Sivak, P. A. Sivak, V. A. Romanov, and V. M. Chernov, Hydrogen diffusion in the elastic fields of dislocations in iron, Phys. At. Nucl. **79**, 1199 (2016).
[17] I. G. Margvelashvili and Z. K. Saralidze, Influence of an elastic field of a dislocation on steady-state diffusion fluxes of point defects, Fiz. Tverd. Tela **15**, 2665 (1973) [Sov. Phys. Solid. State **15**, 1774 (1974)].
[18] W. G. Wolfer and M. Ashkin, Diffusion of vacancies and interstitials to edge dislocations, J. Appl. Phys. **47**, 791 (1975).
[19] A. D. Brailsford and R. Bullough, The theory of sink strengths, Philos. Trans. R. Soc. London **302**, 87 (1981).
[20] H. R. Paneth, The mechanism of self-diffusion in alkali metals, Phys. Rev. **80**, 708 (1950).
[21] P. Ehrhart, The configuration of atomic defects as determined from scattering studies, J. Nucl. Mater. **69**, 200 (1978).
[22] T. D. Swinburne, P.-W. Ma, and S. L. Dudarev, Low temperature diffusivity of self-interstitial defects in tungsten, New J. Phys. **19**, 073024 (2017).
[23] A. Seeger, Diffusion and thermal conversion of crowdions, Phys. Status Solidi **38**, 235 (1970).
[24] P. Ehrhart, P. Jung, H. Schultz, and H. Ullmaier, *Atomic Defects in Metals*, edited by H. Ullmaier (Springer-Verlag, Berlin, 1991), Vol. 25.
[25] H. Schultz, Defect parameters of b.c.c. metals: group-specific trends, Mater. Sci. Eng.: A **141**, 149 (1991).
[26] F. Dausinger and H. Schultz, Long-Range Migration of Self-Interstitial Atoms in Tungsten, Phys. Rev. Lett. **35**, 1773 (1975).
[27] T. Amino, K. Arakawa, and H. Mori, Activation energy for long-range migration of self-interstitial atoms in tungsten obtained by direct measurement of radiation-induced point-defect clusters, Philos. Mag. Lett. **91**, 86 (2011).
[28] F. W. Young Jr., Interstitial mobility and interactions, J. Nucl. Mater. **69**, 310 (1978).
[29] C.-C. Fu, F. Willaime, and P. Ordejón, Stability and Mobility of Mono- and Di-Interstitials in α-Fe, Phys. Rev. Lett. **92**, 175503 (2004).
[30] D. Nguyen-Manh, A. P. Horsfield, and S. L. Dudarev, Self-interstitial atom defects in bcc transition metals: Group-specific trends, Phys. Rev. B **73**, 020101 (2006).
[31] P. M. Derlet, D. Nguyen-Manh, and S. L. Dudarev, Multiscale modeling of crowdion and vacancy defects in body-centered-cubic transition metals, Phys. Rev. B **76**, 054107 (2007).
[32] U. Breier, W. Frank, C. Elsässer, M. Fähnle, and A. Seeger, Properties of monovacancies and self-interstitials in bcc Na: An *ab initio* pseudopotential study, Phys. Rev. B **50**, 5928 (1994).
[33] R. Benedek, L. H. Yang, C. Woodward, and B. I. Min, Formation energy and lattice relaxation for point defects in Li and Al, Phys. Rev. B **45**, 2607 (1992).
[34] R. Pawellek, M. Fähnlet, C. Elsässer, K.-M. Ho, and C.-T. Chan, First-principles calculation of the relaxation around a vacancy and the vacancy formation energy in BCC Li, J. Phys.: Condens. Matter **3**, 2451 (1991).
[35] W. Frank, U. Breier, C. Elsässer, and M. Fähnle, Properties of monovacancies and self-interstitials in bcc Li: An *ab initio* pseudopotential study, Phys. Rev. B **48**, 7676 (1993).
[36] W. Frank, U. Breier, C. Elsässer, and M. Fähnle, First-Principles Calculations of Absolute Concentrations and Self-Diffusion Constants of Vacancies in Lithium, Phys. Rev. Lett. **77**, 518 (1996).
[37] V. Schott, M. Fähnle, and P. A. Madden, Theory of self-diffusion in alkali metals: I. Results for monovacancies in Li, Na, and K, J. Phys.: Condens. Matter **12**, 1171 (2000).
[38] U. Breier, V. Schott, and M. Fähnle, *Ab initio* calculation of formation and migration volumes for vacancies in Li and Na, Phys. Rev. B **55**, 5772 (1997).
[39] P. Olsson, C. Domain, and J. Wallenius, *Ab initio* study of Cr interactions with point defects in bcc Fe, Phys. Rev. B **75**, 014110 (2007).
[40] P. Olsson, *Ab initio* study of interstitial migration in Fe-Cr alloys, J. Nucl. Mater. **386**, 86 (2009).
[41] P.-W. Ma and S. L. Dudarev (unpublished).
[42] S. L. Dudarev, D. R. Mason, E. Tarleton, P.-W. Ma, and A. E. Sand, A multi-scale model for stresses, strains and swelling of reactor components under irradiation, Nucl. Fusion **58**, 126002 (2018).
[43] T. Jourdan, Simulation of macroscopic systems with non-vanishing elastic dipole components, arXiv:1811.11837.
[44] G. Kresse and J. Hafner, *Ab initio* molecular dynamics for liquid metals, Phys. Rev. B **47**, 558 (1993).
[45] G. Kresse and J. Hafner, *Ab initio* molecular-dynamics simulation of the liquid-metal-amorphous-semiconductor transition in germanium, Phys. Rev. B **49**, 14251 (1994).
[46] G. Kresse and J. Furthmüller, Efficiency of *ab initio* total energy calculations for metals and semiconductors using a plane-wave basis set, Comput. Mat. Sci. **6**, 15 (1996).
[47] G. Kresse and J. Furthmüller, Efficient iterative schemes for *ab initio* total-energy calculations using a plane-wave basis set, Phys. Rev. B **54**, 11169 (1996).

[48] P. E. Blöchl, Projector augmented-wave method, Phys. Rev. B **50**, 17953 (1994).
[49] G. Kresse, and D. Joubert, From ultrasoft pseudopotentials to the projector augmented-wave method, Phys. Rev. B **59**, 1758 (1999).
[50] J. P. Perdew, K. Burke, and M. Ernzerhof, Generalized Gradient Approximation Made Simple, Phys. Rev. Lett. **77**, 3865 (1996); **78**, 1396 (1997).
[51] R. Armiento and A. E. Mattsson, Functional designed to include surface effects in self-consistent density functional theory, Phys. Rev. B **72**, 085108 (2005).
[52] A. E. Mattsson and R. Armiento, Implementing and testing the AM05 spin density functional, Phys. Rev. B **79**, 155101 (2009).
[53] A. E. Mattsson, R. Armiento, J. Paier, G. Kresse, J. M. Wills, and T. R. Mattsson, The AM05 density functional applied to solids, J. Chem. Phys. **128**, 084714 (2008).
[54] R. Hafner, D. Spišák, R. Lorenz, and J. Hafner, Magnetic ground state of Cr in density-functional theory, Phys. Rev. B **65**, 184432 (2002).
[55] S. Cottenier, B. De Vries, J. Meersschaut, and M. Rots, What density-functional theory can tell us about the spin-density wave in Cr, J. Phys.: Condens. Matter **14**, 3275 (2002).
[56] H. C. Herper, E. Hoffmann, and P. Entel, *Ab initio* full-potential study of the structural and magnetic phase stability of iron, Phys. Rev. B **60**, 3839 (1999).
[57] P.-W. Ma, S. L. Dudarev, and J. S. Wróbel, Dynamic simulation of structural phase transitions in magnetic iron, Phys. Rev. B **96**, 094418 (2017).
[58] L. D. Landau and E. M. Lifshitz, *Quantum Mechanics: Non-Relativistic Theory* (Pergamon Press, Oxford, 1991), pp. 267–271.
[59] Y. Le Page and P. Saxe, Symmetry-general least-squares extraction of elastic data for strained materials from *ab initio* calculations of stress, Phys. Rev. B **65**, 104104 (2002).
[60] R. P. Feynman, Forces in molecules, Phys. Rev. **56**, 340 (1939).
[61] G. Mills, H. Jonsson, and G. K. Schenter, Reversible work transition state theory: Application to dissociative adsorption of hydrogen, Surf. Sci. **324**, 305 (1995).
[62] H. Jonsson, G. Mills, and K. W. Jacobsen, Nudged elastic band method for finding minimum energy paths of transitions, in *Classical and Quantum Dynamics in Condensed Phase Simulations*, edited by B. J. Berne, G. Ciccotti, and D. F. Coker (World Scientific, Singapore, 1998).
[63] C. H. Rycroft, Voro++: A three-dimensional Voronoi cell library in C++, Chaos **19**, 041111 (2009).
[64] H. C. Nash and C. S. Smith, Single-crystal elastic constants of lithium, J. Phys. Chem. Solids **9**, 113 (1959).
[65] C. Kittel, *Introduction to Solid State Physics*, 7th ed. (John Wiley & Sons, Inc., New York, 1996).
[66] R. H. Martinson, Variation of the elastic constants of sodium with temperature and pressure, Phys. Rev. **178**, 902 (1969).
[67] W. R. Marquardt and J. Trivisonno, Low temperature elastic constants of potassium, J. Phys. Chem. Solids **26**, 273 (1965).
[68] E. J. Gutman and J. Trivisonno, Temperature dependence of the elastic constants of rubidium, J. Phys. Chem. Solids **28**, 805 (1967).
[69] F. J. Kollarits and J. Trivisonno, Single-crystal elastic constants of cesium, J. Phys. Chem. Solids **29**, 2133 (1968).
[70] U. Buchenau, M. Heiroth, H. R. Schober, J. Evers, and G. Oehlinger, Lattice dynamics of strontium and barium, Phys. Rev. B **30**, 3502 (1984).
[71] M. W. Finnis and J. E. Sinclair, A simple empirical N-body potential for transition metals, Philos. Mag. A **50**, 45 (1984).
[72] S. B. Palmer and E. W. Lee, The elastic constants of chromium, Philos. Mag. A **24**, 311 (1971).
[73] J. A. Rayne and B. S. Chandrasekhar, Elastic constants of iron from 4.2 to 300K, Phys. Rev. **122**, 1714 (1961).
[74] B. Gurrutxaga-Lerma, D. S. Balint, D. Dini, and A. P. Sutton, Elastodynamic image forces on dislocations, Proc. R. Soc. London A **471**, 20150433 (2015).
[75] B. Gurrutxaga-Lerma, D. S. Balint, D. Dini, and A. P. Sutton, A dynamic discrete dislocation plasticity study of elastodynamic shielding of stationary cracks, J. Mech. Phys. Solids **98**, 1 (2017).
[76] J. M. Rickman and R. LeSar, Finite-temperature dislocation interactions, Phys. Rev. B **64**, 094106 (2001).